

11 11 7 11
33743
C-128
490/10
(2)

12/11/11 11/11/11

Low Reynolds Number $k-\epsilon$ and Empirical Transition Models for Oscillatory Pipe Flow and Heat Transfer

Christopher Bauer

Master of Science in Mechanical Engineering

Wroclaw Polytechnic University

June, 1991

submitted in partial fulfillment of requirements for the degree

MASTER OF SCIENCE IN MECHANICAL ENGINEERING

at the

CLEVELAND STATE UNIVERSITY

November, 1993

N95-33496

Unclas

G3/34 0058748

(NASA-TM-109785) LOW REYNOLDS
NUMBER KAPPA-EPSILON AND EMPIRICAL
TRANSITION MODELS FOR OSCILLATORY
PIPE FLOW AND HEAT TRANSFER M.S.
Thesis (NASA. Lewis Research
Center) 99 p

This thesis has been approved for the
Department of Mechanical Engineering and the
College of Graduate Studies by

Mounir Ibrahim
Thesis Committee Chairperson

Mech Engrg 12/8/93
Department / Date

Edward G. Keshock

MECH. ENG. 12/8/93
Department / Date

Legend

NASA/ISVERDUP 8-DEC-93
Department / Date

ORIGINAL PAGE IS
OF POOR QUALITY

ACKNOWLEDGEMENTS

I would like to thank my thesis advisor, Dr. Mounir Ibrahim, for his valuable advice, encouragement and guidance throughout the course of this research. His commitment and interest in this project motivated me greatly and his contribution helped me accomplish this work.

I wish to thank Dr. Terry Simon of University of Minnesota for providing me with the experimental data, before it has been published.

I wish to thank Mr. Roy Tew of NASA Lewis Research Center for his guidance, for computer time on the NASA systems and for providing me with an ideal working environment.

I would like to express my appreciation to Dr. Edward Keshock, for inviting me to Cleveland State University and providing me the opportunity to join the graduate program.

Finally, I would like to acknowledge my wife, M.D. Dorota Bauer, for her caring support and understanding of my work.

Low Reynolds Number $k-\epsilon$ and Empirical Transition Models
for Oscillatory Pipe Flow and Heat Transfer

Christopher Bauer

ABSTRACT

Stirling engine heat exchangers are shell-and-tube type with oscillatory flow (zero-mean velocity) for the inner fluid. This heat transfer process involves laminar-transition-turbulent flow motions under oscillatory flow conditions. A low Reynolds number $k-\epsilon$ model, (Lam-Bremhorst form), was utilized in the present study to simulate fluid flow and heat transfer in a circular tube. An empirical transition model was used to activate the low Reynolds number $k-\epsilon$ model at the appropriate time within the cycle for a given axial location within the tube. The computational results were compared with experimental flow and heat transfer data for; (1) velocity profiles, (2) kinetic energy of turbulence, (4) skin friction factor, (4) temperature profiles, and (5) wall heat flux. The experimental data were obtained for flow in a tube (38 mm diameter and 60 diameter long), with the maximum Reynolds number based on velocity being $Re_{max} = 11840$, a dimensionless frequency (Valensi number) of $Va = 80.2$, at three axial locations

$X/D = 16, 30$ and 44 . The agreement between the computations and the experiment is excellent in the laminar portion of the cycle and good in the turbulent portion. Moreover, the location of transition was predicted accurately. The Low Reynolds Number $k-\epsilon$ model, together with an empirical transition model, is proposed herein to generate the wall heat flux values at different operating parameters than the experimental conditions. Those computational data can be used for testing the much simpler and less accurate one dimensional models utilized in 1-D Stirling Engine design codes.

TABLE OF CONTENTS

ACKNOWLEDGEMENTS	iii
ABSTRACT	iv
TABLE OF CONTENTS	vi
LIST OF TABLES	ix
LIST OF FIGURES	x
NOMENCLATURE	xiii
CHAPTER I Statement of the Problem	1
(1.1) Introduction	1
(1.2) Literature Review	4
(1.3) Outline of This Work	8
CHAPTER II Mathematical Description of The Physical Phenomenon ...	9
(2.1) Governing Equations	9
(2.2) Basic Assumptions	12
(2.3) Dimensional Analysis (Similarity Parameters)	13
(2.4) Boundary Conditions	16
CHAPTER III Numerical Method for the Solution of the Governing	
Equations	19
(3.1) Discretization Method	20
(3.2) Solution Procedure	23

(3.3) Code Modification for Oscillating Flow	24
CHAPTER IV Turbulence Modeling of Oscillatory Flow	26
(4.1) Comparison of Various Turbulence Models	26
(4.2) The Lam Bremhorst k - ϵ Model	28
(4.2.1) The Damping functions in the Lam Bremhorst k - ϵ Model .	29
(4.2.2) The Boundary Conditions in the k - ϵ Model	32
(4.3) Evaluation the Constants in the k - ϵ Model	33
(4.4) The Empirical Transition Model	35
CHAPTER V Code Validation with Pipe Flow under Steady State Conditions	37
(5.1) Fully Developed Flow	38
(5.2) Heat Transfer	45
CHAPTER VI Numerical Results and Comparison with Experiment	46
(6.1) Description of the Experiment	47
(6.2) Fluid Flow Predictions	49
(6.2.1) Velocity Profiles	50
(6.2.2) Turbulent Kinetic Energy	59
(6.2.3) Skin Friction Factor	60
(6.3) Heat Transfer	67
(6.3.1) Description of the Experiment	67
(6.3.2) Numerical Predictions	67
(6.3.3) Temperature Profiles	69

(6.3.4) The Wall Heat Flux	70
CHAPTER VII Closure	78
(7.1) Summary and Conclusion	78
(7.2) Suggestion for Further Research	82
REFERENCES	83

LIST OF TABLES

<i>Table I</i>	Interpretations of ϕ , Γ_ϕ and S_ϕ for the governing equations	19
<i>Table II</i>	Terms of k and ϵ equations	28
<i>Table III</i>	The damping functions in the turbulence modeling	31
<i>Table IV</i>	Boundary conditions for the high Reynolds number and low Reynolds number models	32
<i>Table V</i>	Turbulent modeling constants	34
<i>Table VI</i>	The operating parameters	47
<i>Table VII</i>	Evaluation of figures 6.3a, b, c.	51
<i>Table VIII</i>	The measurements of the wall temperature	66

LIST OF FIGURES

<i>Figure 1.1.</i>	Quarter Sectional View of NASA's Stirling Space Power Development Engine SPDE	2
<i>Figure 1.2.</i>	Stirling Engine Schematic with Locations of Heat Transfer and Fluid Flow Problems Areas	3
<i>Figure 2.1.</i>	Boundary conditions	16
<i>Figure 3.1.</i>	The staggered grid for three distinctive spatial control volumes	21
<i>Figure 3.2.</i>	Computational domain	22
<i>Figure 3.3.</i>	Control volume arrangement and grid numbering	22
<i>Figure 4.1.</i>	The damping functions in the Lam Bremhorst model	32
<i>Figure 5.1.</i>	Dimensionless velocity profile for the steady state fully developed pipe flow at $Re = 500$	41
<i>Figure 5.2.</i>	Dimensionless velocity profile for the steady state fully developed pipe flow at $Re = 5000$	42
<i>Figure 5.3.</i>	Dimensionless velocity profile for the steady state fully developed pipe flow at $Re = 15000$	43
<i>Figure 5.4.</i>	Dimensionless velocity profile for the steady state fully developed pipe flow at $Re = 50000$	44
<i>Figure 6.1.</i>	The oscillating flow facility at the University of Minnesota	47
<i>Figure 6.2a.</i>	Normalized velocity profile for oscillatory pipe flow at $X/D = 16$. .	53
<i>Figure 6.2b.</i>	Normalized velocity profile for oscillatory pipe flow at $X/D = 30$. .	54
<i>Figure 6.2c.</i>	Normalized velocity profile for oscillatory pipe flow at $X/D = 44$. .	55
<i>Figure 6.3a.</i>	Dimensionless velocity (U^*) profile for oscillatory pipe flow at $X/D = 16$	56

Figure 6.3b.	Dimensionless velocity (U^*) profile for oscillatory pipe flow at $X/D = 30$	57
Figure 6.3c.	Dimensionless velocity (U^*) profile for oscillatory pipe flow at $X/D = 44$	58
Figure 6.4a.	Turbulent kinetic energy (k) profile for oscillatory pipe flow at $X/D = 16$	61
Figure 6.4b.	Turbulent kinetic energy (k) profile for oscillatory pipe flow at $X/D = 30$	62
Figure 6.4c.	Turbulent kinetic energy (k) profile for oscillatory pipe flow at $X/D = 44$	63
Figure 6.5.	Skin friction factor (C_f) prediction from the Turbulent Model, the Transition Model, the Laminar Model and the experiment for oscillatory flow ($Re_{max} = 11840$, $Va = 80.2$, $L/D = 60$) at $X/D = 16, 30, 44$ locations	65
Figure 6.6.	Friction velocity (U^*) prediction from the Turbulent Model, the Transition Model, the Laminar Model and the experiment for oscillatory flow ($Re_{max} = 11840$, $Va = 80.2$, $L/D = 60$) at $X/D = 16, 30, 44$ locations	66
Figure 6.7.	Wall temperature distribution	68
Figure 6.8.	Temperature profile at midplane from the Transition Model prediction and the experiment	73
Figure 6.9.	Temperature profile at a) $X/D = 16$, b) $X/D = 44$	74
Figure 6.10.	The wall heat flux at the midplane	75
Figure 6.11.	The wall heat flux at a) $X/D = 16$, b) $X/D = 44$	76

<i>Figure 6.12.</i> Comparison of the wall heat flux at midplane between the experimental data, 1-D Model and the Transition Model	77
--	----

NOMENCLATURE

A_r	Relative amplitude of fluid motion.
C_f	Skin friction factor.
c_p	Specific Heat of the fluid.
c_1, c_2, c_μ	Turbulence k - ϵ model constants.
D	Diameter of the tube.
f_1, f_2, f_μ	Turbulence k - ϵ model damping functions.
k	Turbulent kinetic energy $k = (1/2)(U'^2 + V'^2 + W'^2)$.
L	Length of the tube.
Nu	Nusselt number.
P	Hydrodynamic pressure in the momentum equations.
Pr	Prandtl number of the fluid.
q''	Heat flux.
r	Radial coordinate distance.
R	Radius of the tube.
Re	Reynolds number.
Re_{max}	Reynolds number based on the maximum velocity (U_{max}).
R_t	Turbulence Reynolds number $R_t = k^2/\nu\epsilon$.
R_y	Turbulence Reynolds number $R_y = \sqrt{k}y/\nu$.
t	Time.
T	Temperature.
TI	Turbulence intensity [%].
St	Stanton number.
Str	Strouhal number.
U	Axial velocity in the x direction.
U^*	Dimensionless velocity.
U/U_c	Normalized velocity by center line velocity.
V	Normal velocity of the fluid in the r direction.
U^*	Friction velocity.
Va	Valensi Number $Va = \omega D^2/4\nu$.
X/D	Location in the tube.
y	Distance from the wall $y = R-r$.
Y^*	Dimensionless distance from the wall.

SUPERSCRIPTS

/	Fluctuating component.
-	Phase-averaged quantity.

SUBSCRIPTS

<i>in</i>	Inlet condition.
<i>max</i>	Maximum value during the cycle.
<i>L</i>	Laminar.
<i>T</i>	Turbulent.
<i>ref</i>	Reference value.
<i>Sk</i>	Base on sink temperature.
<i>U</i>	Base on axial velocity.
<i>V</i>	Base on radial velocity.
<i>w</i>	Boundary condition at the wall.

GREEK SYMBOLS

ϵ	Dissipation rate of turbulence.
λ	Thermal conductivity.
Γ	Diffusion coefficient.
$\sigma_k, \sigma_\epsilon, \sigma_T$	Turbulent Prandtl number for k , ϵ and T .
θ	Crank angle.
μ	Dynamic viscosity of the fluid.
μ_t	Turbulent dynamic viscosity of the fluid.
ν	Kinematic viscosity of the fluid.
ρ	Density of the fluid.
τ	Shear stress.
Φ	Viscous dissipation function.
ω	Angular frequency in [rad/sec].

ORIGINAL PAGE IS
OF POOR QUALITY

CHAPTER I

Statement of the Problem

(1.1) Introduction

Since James Watt developed Steam Engine at the end of eighteenth century, people have been working very hard to develop new forms of engines to produce mechanical power. Starting from steam engines and numerous forms of internal combustion engines, presently researchers are working on developing the Stirling engine.

The Stirling engine is a device whose operation is based upon the thermodynamic cycle proposed by Robert Stirling (1815), whose theoretical efficiency is the same as that of Carnot cycle. Its recent designs have been efficient, reliable, operating with a low noise level with a very long life. Furthermore, it can work in any atmospheric conditions and is pollution free. An interesting feature of the Stirling machine is that it can be designed to work as an electrical or mechanical power generator, or as a cooling machine (acting as a refrigeration device or as a heat pump for space heating). An important feature is that it can be driven by any heat source available in a particular application,

such as solar energy or even heat produced by the human body.

There is a wide range of possible applications for Stirling machines, from a power source for future space stations, to a reliable motor for agricultural machinery, or a Stirling engine powered artificial heart. As an example, the view of one of the NASA's research engines design for space applications is presented in Figure 1.1.

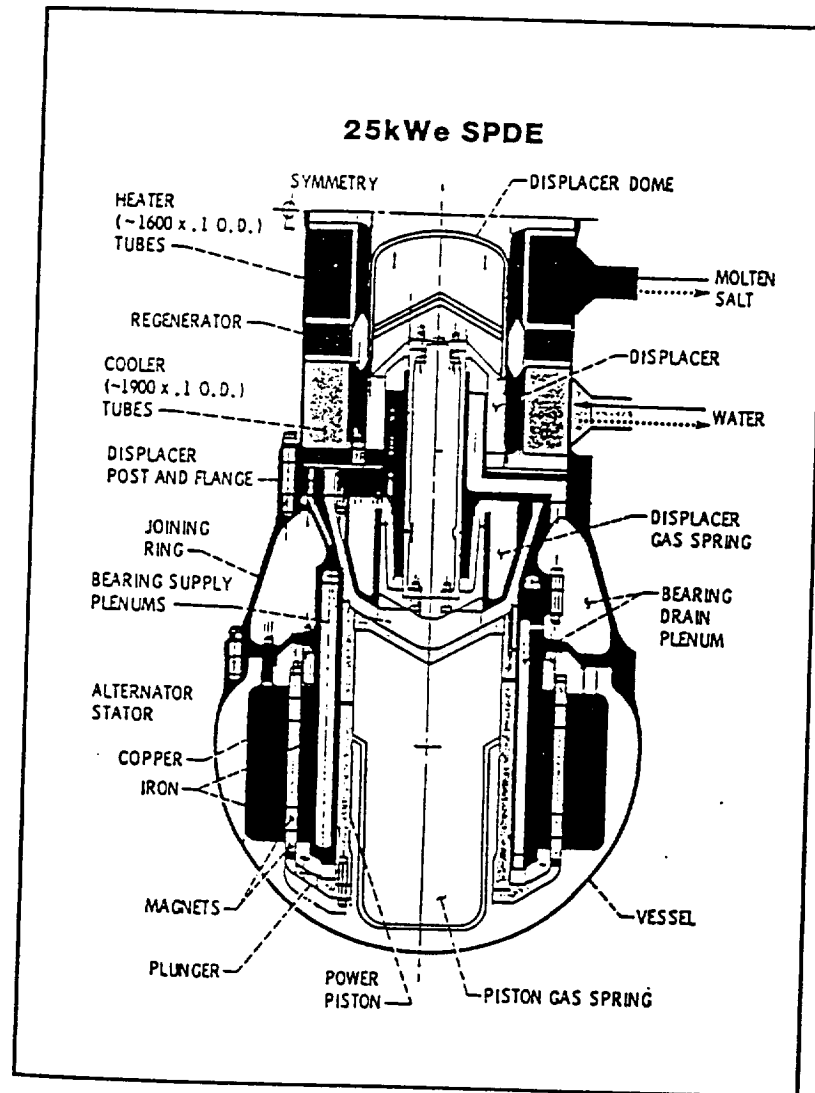


Figure 1.1. Quarter Sectional View of NASA's Stirling Space Power Development Engine SPDE.

The most important aspect for the future development of Stirling engines is a very

careful design of all parts where heat transfer process is taking place. Such design can be aided greatly by using computer simulation. The new computer programs presently used to design and model Stirling engines need improvement for application to wide variety of Stirling engines. Therefore, there is a strong need for better codes and more accurate information about flow field and heat transfer phenomena in the laminar, transition and turbulent regions of the flow. Because of the and complexity of the problem, which requires that much data be stored and processed, a CRAY supercomputer was used for the calculations.

A schematic view of the Stirling engine, with locations of heat transfer and fluid flow problem areas identified, is presented in Figure 1.2.

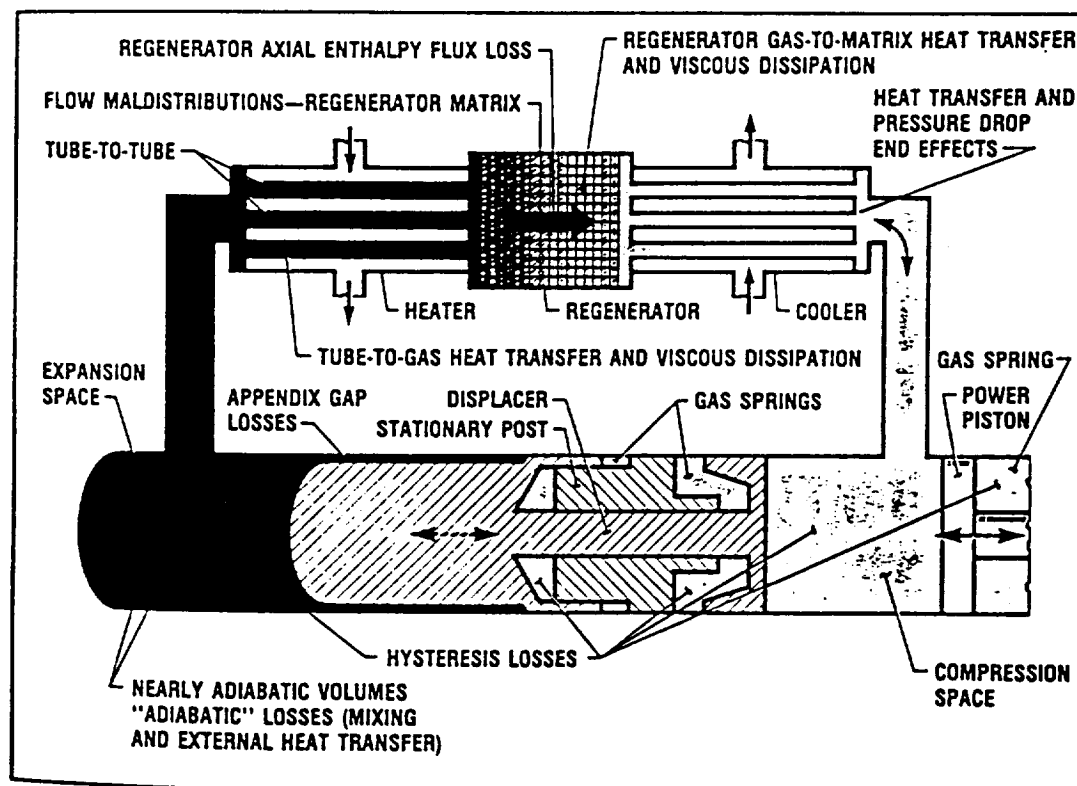


Figure 1.2. Stirling Engine Schematic with Locations of Heat Transfer and Fluid Flow Problems Areas.

A number of experiments have been performed at the University of Minnesota to understand laminar, transition and turbulent flows. In parallel with those experiments, several numerical simulations of oscillatory flow with heat transfer have also been performed, (Patankar (1992); Koehler (1990); Ibrahim et. al. (1992); Kannapareddy (1993)). It is obvious that experiments are very difficult and expensive. Therefore, using a simulation program, a wider range of operating conditions in various geometrical configurations can be studied.

Adding to the basic knowledge and understanding of transition and turbulent oscillating flow, present study can contribute to the development of a simulation program and the improvement of Stirling engine designs.

(1.2) Literature Review

Many studies discussing oscillating flow problems exist in the literature. In order to understand the character of this type of flow, previous experiments and numerical simulations will be discussed further here.

Many different types of unsteady flow are characterized in the literature. Among them, are the periodic unsteady flows, such as pulsating flow and oscillating flow will be described here. These two types of cyclic flows can first be characterized by the value of the mean flow velocity. In oscillating flow, which can be a specific case of pulsating flow, the mean velocity within one cycle is zero. This means that the net mass transfer within a cycle across any tube cross-section is also zero. In pulsating flow, these conditions are not necessarily satisfied. Pulsating flow can be defined as a superposition

of a steady mean and an oscillatory flow.

Richardson and Tyler (1929) first studied steady and oscillating flows. By examination of the sound waves in resonators, they found the velocity maxima not far away from the wall.

Ohmi, et. al. (1982) examined a wide range from fully laminar to fully turbulent oscillating flows. They found that the velocity profiles in the laminar part of the cycle agree with the theoretical oscillating flow solution. But in the turbulent part of the cycle, they found that the velocity profiles agree well with the $1/7$ power law for steady turbulent flow.

Iguchi et. al. (1982) studied liquid oscillation in a U-tube. They determined that the change from laminar to transition flow takes place where the amplitude of oscillation begins to deviate from that predicted by the analytical solution for laminar flow. On the other hand, the change from transition to turbulent flow appears when the measured amplitudes of oscillation match those computed with the $1/7$ power law profile. However, it is difficult to directly compare their prediction with the transition regime location in a straight tube, because they used U-type bend tube, rather than straight tube.

Hino, et. al. (1983) conducted an extensive study of oscillating flow in a rectangular duct. They focused on the turbulence structure of the flow, wall shear stresses, Reynolds shear stresses, turbulent fluctuations, and coherent structure of turbulence. They found that in the accelerating phase turbulence is triggered near the wall but suppressed, while in the deceleration phase, turbulence is generated vigorously in the near wall region and spreads to the core flow.

In his experimental work, Seume (1988) defines the criterion for transition as a rapid increase in the measured rms velocity fluctuations. He verifies that in oscillating flow, the critical Reynolds number depends on the Valensi number, and describes two mechanisms that trigger turbulence. First, transition can be caused by an incoming fluid carrying a turbulent slug, and second, can be triggered by unstable boundary layer growth at higher Reynolds numbers.

Koehler (1990) used the low Reynolds number k - ϵ turbulence model to numerically predict the oscillating flow and associated heat transfer. He identified the Lam-Bremhorst form of the k - ϵ model (Lam and Bremhorst (1981)), as suitable for oscillating flow calculations and compared mean velocity profiles and fluctuations with experimental results obtained from the oscillating flow test facility at the University of Minnesota. He showed that the model has the capability to qualitatively correctly predict the transition to turbulence in quasi-steady and accelerated pipe flow. He pointed out that the inflow boundary condition should be theoretically, or, if possible, experimentally investigated in order to enable the prediction of traveling a turbulent slug downstream of the flow.

Eckmann and Grotberg (1991) studied the transition to turbulence in oscillating flow in a pipe over a wide range of relative amplitude of fluid displacement (A_r) and Womersley parameter (α). They used two measurement techniques: hot-film anemometry and laser Doppler velocimetry. They observed that post transition turbulence was confined to a thin region near the wall for Reynolds numbers (based on

the Stokes-layer thickness $Re_\delta = U_{mean} \delta / \nu$) greater than 500 and high frequencies.

Ahn and Ibrahim (1992) used the high Reynolds number $k-\epsilon$ turbulence model to examine oscillating flows under an operating conditions typical of Stirling power systems. Their results were compared with experimental data from University of Minnesota. In the laminar flow regime their predictions matched the data with relatively high accuracy; in the transition and turbulent regimes the computations matched the data with acceptable error. However, they concluded that further improvement in the turbulence modeling was necessary.

Ibrahim and al. (1992) proposed an empirical model for transition to turbulence in oscillatory flows, in straight tubes. They used the momentum thickness Reynolds number (Re_{δ_2}) at the point of transition to turbulence expressed in terms of turbulent intensity (II). From that model, the position of the turbulent slug from the tube entrance could be determined for different angular positions within the cycle.

In experiments at the University of Minnesota documented by Seume et al. (1992), oscillating flow study at the SPDE Stirling engine operating conditions were conducted. They measured and documented the axial and radial components of ensemble averaged velocity, rms velocity fluctuation, and dominant Reynolds shear stress, at various radial position for four axial locations. From this data, the laminar, the transition and the turbulent regions within the cycle could be identified and isolated. Their detailed measurements are useful in characterizing attributes of oscillating flow, including flow phenomena observed in the near wall region at flow reversal and during

the transition process.

(1.3) Outline of Present Study

First, the problem to be studied is mathematically described. All governing equations, the boundary conditions and important assumptions are introduced. Next, the numerical methods for solving the system of governing equations are presented. Then, the turbulence modeling is discussed. Following this, in order to validate code performance the steady state flow calculations are given. Finally, the results of the oscillating fluid flow and associated heat transfer are compared with experimental data and discussed.

CHAPTER II

Mathematical Description of the Physical Phenomenon

The description of the governing equations for all dependent variables, the fundamental assumptions and the boundary conditions for solving the oscillatory flow with heat transfer problem is given in this chapter. Also, several nondimensional variables which not only simplify the problem but also provide the natural scale for the boundary conditions, physical properties, and geometry are presented.

(2.1) Governing Equation

The governing differential equation expressing the conservation of mass, momentum and energy for a continuum are listed below. In k - ϵ turbulence modeling, two additional equations for turbulent kinetic energy (k -equation) and dissipation rate of turbulence (ϵ -equation) are used. All of these are given in the axisymmetric

coordinate system used for unsteady flow over an infinitesimal control volume, (see Peric and Scheuerer (1989) and Munson et. al. (1990)).

Continuity Equation

From the conservation of mass principle the following formulation for the continuity equations results.

$$\frac{\partial U}{\partial x} + \frac{1}{r} \frac{\partial}{\partial r}(rV) = 0 \quad (2.1)$$

Momentum Equations

The conservation of momentum yields two equations in the x and r directions respectively.

x -Momentum

$$\rho \frac{\partial U}{\partial t} + \rho U \frac{\partial U}{\partial x} + \rho V \frac{\partial U}{\partial r} = -\frac{\partial P^*}{\partial x} + \frac{\partial}{\partial x}(\mu_{eff} \frac{\partial U}{\partial x}) + \frac{1}{r} \frac{\partial}{\partial r}(r \mu_{eff} \frac{\partial U}{\partial r}) \quad (2.2)$$

r -Momentum

$$\rho \frac{\partial V}{\partial t} + \rho U \frac{\partial V}{\partial x} + \rho V \frac{\partial V}{\partial r} = -\frac{\partial P^*}{\partial r} + \frac{\partial}{\partial x}(\mu_{eff} \frac{\partial V}{\partial x}) + \frac{1}{r} \frac{\partial}{\partial r}(r \mu_{eff} \frac{\partial V}{\partial r}) - \mu_{eff} \frac{V}{r^2} \quad (2.3)$$

The modified pressure P^* is equal to

$$P^* = P + \frac{2}{3} \mu_{eff} \left(\frac{\partial U}{\partial x} + \frac{\partial V}{\partial r} + \frac{V}{r} \right) \quad (2.4)$$

and P is the hydrodynamic pressure.

Energy Equation

$$\rho \frac{\partial T}{\partial t} + \rho U \frac{\partial T}{\partial x} + \rho V \frac{\partial T}{\partial r} = \frac{\partial}{\partial x} \left[\left(\frac{\mu}{Pr} + \frac{\mu_T}{\sigma_T} \right) \frac{\partial T}{\partial x} \right] + \frac{1}{r} \frac{\partial}{\partial r} \left[\left(\frac{\mu}{Pr} + \frac{\mu_T}{\sigma_T} \right) \frac{\partial T}{\partial r} \right] + S_T \quad (2.5)$$

where S_T is a source or sink term, representing e.g. heat generation by chemical reactions. In present study S_T is assumed to be zero.

Turbulent Kinetic Energy k -Equation

$$\rho \frac{\partial k}{\partial t} + \rho U \frac{\partial k}{\partial x} + \rho V \frac{\partial k}{\partial r} = \frac{\partial}{\partial x} \left[\left(\mu + \frac{\mu_T}{\sigma_k} \right) \frac{\partial k}{\partial x} \right] + \frac{1}{r} \frac{\partial}{\partial r} \left[\left(\mu + \frac{\mu_T}{\sigma_k} \right) \frac{\partial k}{\partial r} \right] + \rho G - \rho \varepsilon \quad (2.6)$$

where $k = (1/2) \overline{(U'^2 + V'^2 + W'^2)}$

Dissipation Rate of Turbulence ε -Equation

$$\rho \frac{\partial \varepsilon}{\partial t} + \rho U \frac{\partial \varepsilon}{\partial x} + \rho V \frac{\partial \varepsilon}{\partial r} = \frac{\partial}{\partial x} \left[\left(\mu + \frac{\mu_T}{\sigma_\varepsilon} \right) \frac{\partial \varepsilon}{\partial x} \right] + \frac{1}{r} \frac{\partial}{\partial r} \left[\left(\mu + \frac{\mu_T}{\sigma_\varepsilon} \right) \frac{\partial \varepsilon}{\partial r} \right] + c_1 f_1 \rho G \frac{\varepsilon}{k} - c_2 f_2 \rho \frac{\varepsilon^2}{k} \quad (2.7)$$

where the generation term G is

$$G = \mu_T \left[2 \left(\frac{\partial U}{\partial x} \right)^2 + 2 \left(\frac{\partial V}{\partial r} \right)^2 + 2 \left(\frac{V}{r} \right)^2 + \left(\frac{\partial U}{\partial r} + \frac{\partial V}{\partial x} \right)^2 \right] \quad (2.8)$$

and using Prandtl Komogorov's expression, the turbulent viscosity is modeled as:

$$\mu_T = \rho c_\mu f_\mu \frac{k^2}{\varepsilon} \quad (2.9)$$

The k -equation and ε -equation with all constants and functions will be fully described in Chapter IV.

(2.2) Basic Assumptions

The geometry of Stirling engine heat exchangers, which are normally of the shell-and-tube type, is complicated. However, for simplicity and for better understanding the basis of the physical phenomena, a straight tube was used in the experiments at University of Minnesota as well as in the computational phase of the present study. Using an axisymmetric coordinate system (x, r, ϕ) , one can assume that there are no changes in the azimuthal direction, and the velocity in this direction is zero:

$$w = 0, \quad \frac{\partial}{\partial \phi} = 0$$

Throughout this work, the fluid is assumed to be Newtonian, incompressible, and a continuum, and. With that in mind and neglecting buoyancy forces, the Navier-Stokes equation takes the following form:

$$\rho \frac{\partial \vec{U}}{\partial t} + \rho \vec{U}(\nabla \vec{U}) = -\nabla P + \nabla(\mu(\nabla \vec{U})) + \nabla(\mu(\nabla \vec{U})^*) \quad (2.11)$$

where the pressure is defined as:

$$P = p + \frac{2}{3}\mu(\nabla \vec{U})$$

Using Fourier's law

$$q = -\lambda(\nabla T) \quad (2.12)$$

the energy equation for an incompressible, constant properties gas, can be written as follows:

$$\rho \frac{\partial T}{\partial t} + \rho \vec{U}(\nabla T) = \nabla\left(\frac{\lambda}{c_p}(\nabla T)\right) + \frac{1}{c_p}\left(\frac{\partial p}{\partial t} + \vec{U}(\nabla p)\right) + \frac{\mu}{c_p} \Phi \quad (2.13)$$

where the viscous dissipation function Φ for a Newtonian fluid in axisymmetric coordinates can be written as:

$$\Phi = 2\left(\frac{\partial U}{\partial x}\right)^2 + 2\left(\frac{\partial V}{\partial r}\right)^2 + 2\left(\frac{V}{r}\right)^2 + \left(\frac{\partial U}{\partial r} + \frac{\partial V}{\partial x}\right)^2 \quad (2.14)$$

The equations (2.1), (2.11), and (2.13) are sufficient to solve for the four independent variables: U , V , T and P . These form the complete set of equations necessary to describe the flow field and heat transfer in oscillating flow. The basic assumptions used to derive the theoretical equations are summarized as follows:

- Axisymmetric geometry.
- Fluid is a continuum, Newtonian fluid with constant properties.
- Fourier heat conduction law, no internal heat sources and no radiation heat transfer.
- No body forces or gravitational effects.

(2.3) Dimensional Analysis (Similarity Parameters)

The following characteristic parameters are generally used to describe the fluid flow and heat transfer in similar systems.

Maximum Reynolds Number (Re_{\max})

One of the most important similarity parameters is a maximum Reynolds number,

which can be describe as follows:

$$Re_{\max} = \frac{\rho U_{\max} D}{\mu}$$

This definition is similar in structure to the well known definition of Reynolds Number, but since the mean velocity U is zero for oscillating flow, the maximum velocity U_{\max} (amplitude velocity) is typically employed.

Valensi Number (Va)

Oscillatory flows are unsteady by definition, so the frequency of oscillation must be defined. In dimensionless form, the frequency of oscillation as a Valensi Number can be described:

$$Va = \frac{\omega D^2}{4\nu}$$

The Valensi Number can be physically interpreted as the ratio of the viscous diffusion time scale $D^2/4\nu$ to the oscillation period $1/\omega$.

Srouhal Number (Str)

The Srouhal Number Str is used to connect the frequency of the oscillating flow with U_{\max} and D and is defined as follows:

$$Str = \frac{\omega D}{U_{\max}}$$

Using earlier definitions of Re_{\max} and Va it takes the form: $Str = \frac{4 Va}{Re_{\max}}$

Relative Amplitude of Fluid Displacement (A_r)

The relative amplitude of fluid displacement, A_r , is a derived parameter that can

be defined as the maximum axial fluid displacement during one cycle divided by the duct length. In the mathematical form,

$$A_r = \frac{2U_{\max}}{\omega L}$$

Using earlier definitions of Re_{\max} and Va , it takes the form:

$$A_r = \frac{1}{2} \frac{D}{L} \frac{Re_{\max}}{Va}$$

For $A_r > 1$ all of the fluid initially contained in the pipe is pushed outside at some time during the cycle;

For $A_r = 1$ all of the fluid initially contained in the pipe is moved the length of the channel;

For $A_r < 1$ from all of the fluid initially contained in the pipe some does not leave for any time during the cycle.

Prandtl Number (Pr)

The well known definition of the Prandtl Number Pr , is:

$$Pr = c_p \frac{\mu}{\lambda} \quad \text{where } \lambda \text{ is used for thermal conductivity.}$$

Geometric Similarity Parameters (X/D) and (D)

The similarity parameters X/D and D are used to describe the geometry of the problem. The dimensionless length X/D , is a well known similarity parameter and will be often used in this work.

(2.4) Boundary Conditions

Since the governing momentum and energy equations are parabolic in time and elliptic in space, they can describe a whole class of fluid flow problems. By specifying boundary conditions for each of the dependent variables along the computational domain, the problem formulation may be completed. Four different types of boundary condition are used herein. They are shown in Figure 2.1.

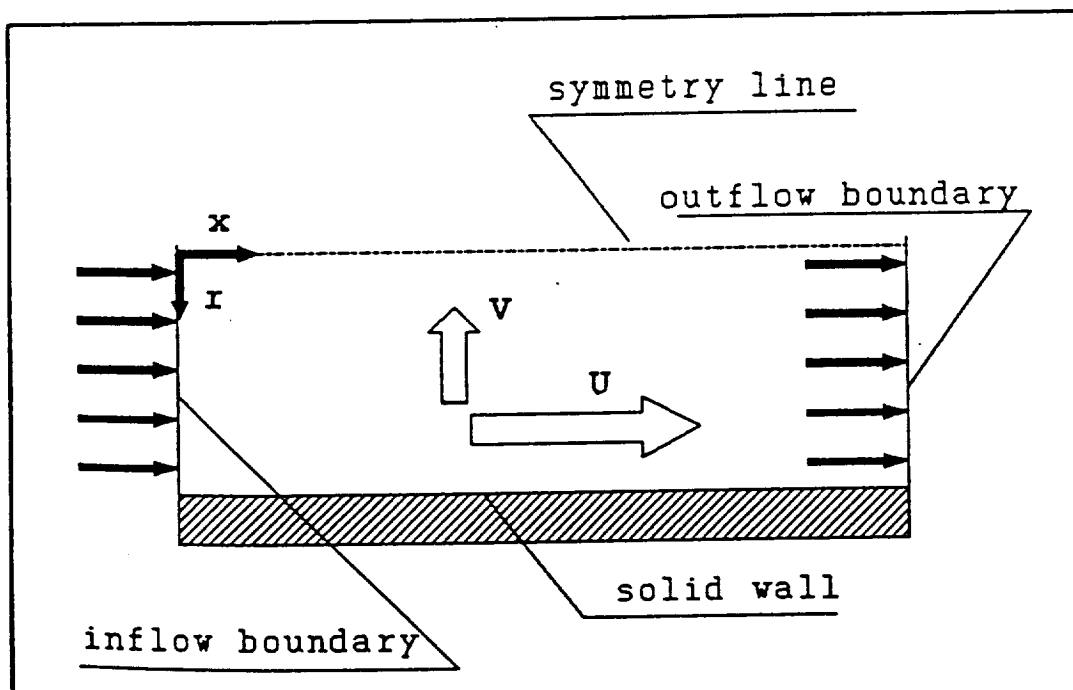


Figure 2.1. Boundary Conditions.

Solid Walls

Along the wall the fluid velocity is zero, assuming a no-slip condition and an impermeable wall. For the energy equation the wall temperature is specified.

$$U = V = \frac{\partial U}{\partial x} = \frac{\partial V}{\partial x} = 0 \quad \text{and} \quad T = T_{\text{wall}}, \quad \frac{\partial T}{\partial x} = 0 \quad (2.15)$$

Axis of Symmetry

At the center line of the tube, which is an axis of symmetry Neumann type boundary conditions are used here.

$$\frac{\partial U}{\partial r} = V = \frac{\partial T}{\partial r} = 0 \quad (2.16)$$

Inlet Plane

Dirichlet type boundary conditions are used on the inlet plane since all values of the dependent variables are specified.

$$U_{\text{in}} = U_{\text{max}} \sin \theta, \quad V_{\text{in}} = 0, \quad T_{\text{in}} = T_{\text{inflow}} \quad (2.17)$$

Outlet Plane

Neumann type boundary conditions are used on the outlet plane, which states in effect that the diffusive fluxes normal to the exit plane can be neglected. Since the values of the dependent variables are not known a priori at these planes the gradients of the dependent variables in a direction normal to the outlet plane are assumed to be zero. Such a situation is valid if the outlet plane is far from the entrance or any recirculating activities.

$$\frac{\partial U}{\partial x} = \frac{\partial V}{\partial x} = \frac{\partial T}{\partial x} = 0 \quad (2.18)$$

It should be noted that by specifying the inlet velocity U_{in} as a time dependent value, (see equation 2.17) the acceleration and deceleration of the fluid is accounted. Simulating the oscillating flows after each half cycle, the outlet plane boundary conditions are used for the inlet plane boundary conditions during the next half cycle. The boundary conditions for additional differential equations are presented in Chapter IV.

CHAPTER III

Numerical Methods for the Solution of the Governing Equations

The governing elliptic partial differential equations together with the boundary conditions can not be solved analytically. However, solutions for this coupled set of equations can be found using numerical methods. Any of the numerical methods of solution consist of two basic steps. First, the computational domain is divided into a number of subdomains. This transforms (discretizes) the partial differential equations into an easy-to-solve set of algebraic equations. Second, this set of algebraic equations has to be solved.

Many methods to discretize partial differential equations have been proposed. Among them, the most widely used are the Finite Difference Method, Finite Element Method and Finite Volume Method.

The code used in present study is based on the C.A.S.T. (Computer Aided Simulation of Turbulent Flows) code developed by Peric and Scheuerer (1989). The Finite Volume Method is used in this code with an ability to handle various flow types, geometries and boundary conditions.

(3.1) Discretization Method

An important step in solving a set of partial differential equations is transforming them into one general transport equation. Next, one common algorithm is needed to solve all dependent variables. Then, we can write for any scalar variable ϕ the transport equation as:

$$\frac{\partial(\rho\phi)}{\partial t} + \frac{\partial}{\partial x}(\rho U\phi - \Gamma_\phi \frac{\partial\phi}{\partial x}) + \frac{1}{r} \frac{\partial}{\partial r}(\rho r V\phi - \Gamma_\phi \frac{\partial\phi}{\partial r}) = S_\phi \quad (3.1)$$

Choosing appropriate quantities for ϕ , Γ_ϕ and S_ϕ from table I, all the transport partial differential equations can be retrieved from equation (3.1).

Equation	ϕ	Γ_ϕ	S_ϕ
Continuity	1	0	0
x Momentum	U	μ_{eff}	$-\frac{\partial P^*}{\partial x}$
r Momentum	V	μ_{eff}	$-\frac{\partial P^*}{\partial r}$
Energy	$c_p T$	$\frac{\mu}{Pr} + \frac{\mu_T}{\sigma_T}$	0
Turbulent Kinetic Energy	k	$\mu + \frac{\mu_T}{\sigma_k}$	$\rho G - \rho \epsilon$
Turbulent Dissipation Rate	ϵ	$\mu + \frac{\mu_T}{\sigma_\epsilon}$	$c_1 f_1 \rho G \frac{\epsilon}{k} - c_2 f_2 \rho \frac{\epsilon^2}{k}$

Table I. Interpretations of ϕ , Γ_ϕ and S_ϕ for the governing equations.

The computational domain is divided into a number of finite control volumes which compose the computational grid. To prevent the probable development of wavelike velocity or pressure fields, a "staggered grid" for velocity U and V has been used. For all other variables, a "normal grid" has been used (see figure 3.1). The values of the dependent variables are evaluated at the centers of their control volumes.

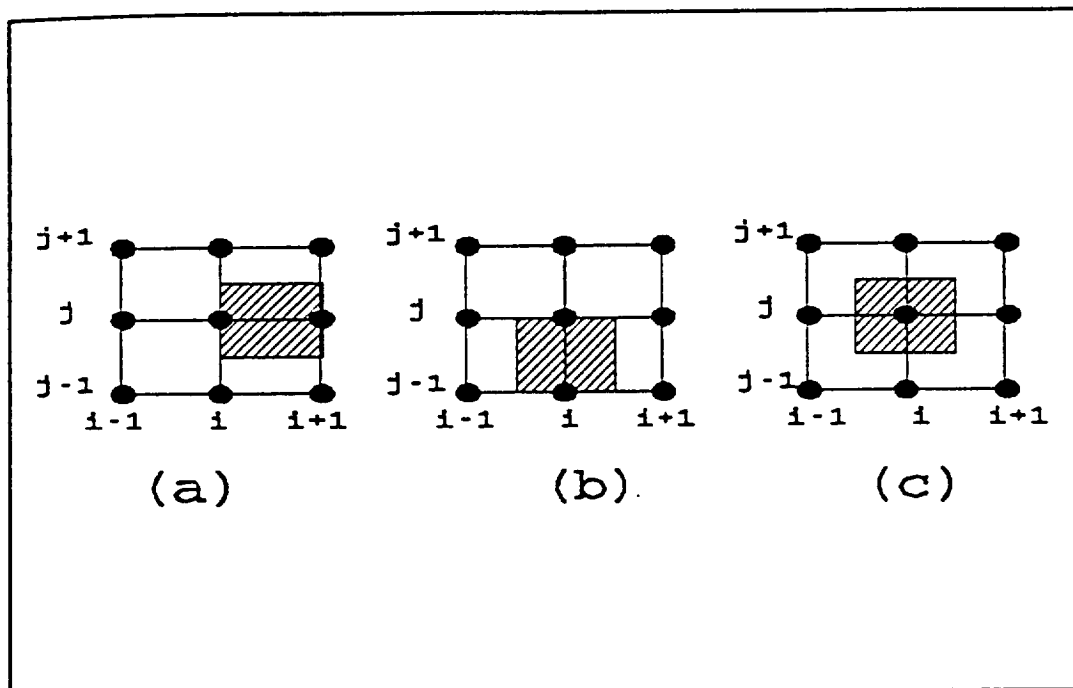


Figure 3.1. The staggered grid for three distinctive spatial control volumes for:
a) x-momentum equation;
b) r-momentum equation;
c) continuity, energy, k - ϵ equations.

Simplified diagrams of a computational domain and grid arrangement, are presented on figures 3.2 and 3.3. For a more detailed explanation refer to Peric and Scheuerer (1989).

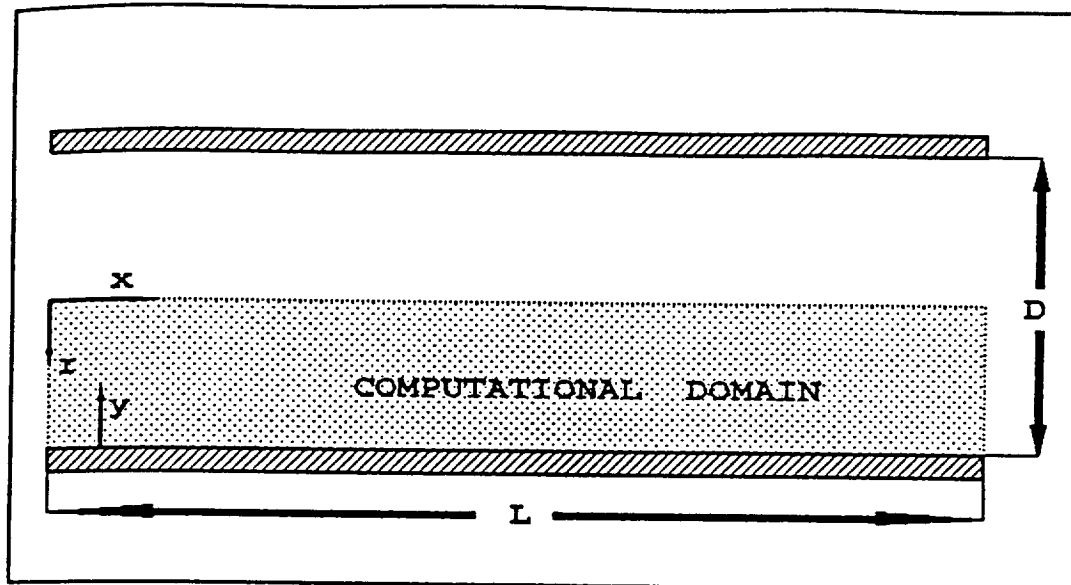


Figure 3.2. Computational domain.

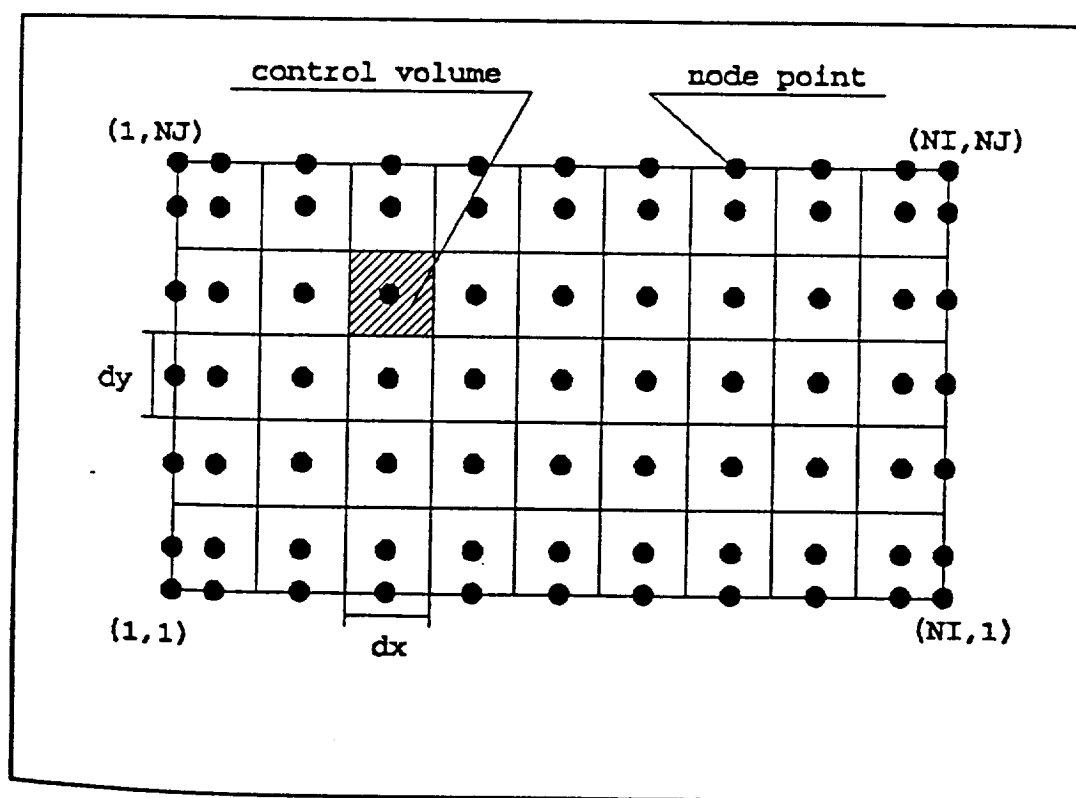


Figure 3.3. Control Volume arrangement and grid numbering.

(3.2) Solution Procedure

The dependent variables are coupled together in the set of governing equations presented in Chapter II. The iterative SIMPLE algorithm (Semi Implicit Method for Pressure Link Equations) developed by Patankar and Spalding (1972) has been implemented in the C.A.S.T. code (Peric and Scheuerer (1989)), and has been used in this study. The SIMPLE algorithm consists of the following steps:

- (step 0) The initialization of all the values for dependent variables are performed in order to evaluate the finite volume coefficients. For unsteady flows, values from the previous time step can be used or the given initial values for the first time step.
- (step 1) The linear equation set is created by assembling the finite volume coefficients of the x -momentum equation. The resulting set is solved giving the velocity field U^* .
- (step 2) The same procedure is performed for the r -momentum equation to give V^* .
- (step 3) As the initially guessed pressure field is most probably wrong, the velocities U^* and V^* will not satisfy the continuity equation. Therefore the next step is to derive pressure and associated velocity and mass flux corrections, so the corrected values will satisfy the continuity and the momentum equations.
- (step 4) If the velocities satisfies the continuity equation, the energy equation can

be solved in an analogous manner as the momentum equations.

(step 5) For turbulent flow, the turbulent kinetic energy k -equation and the

dissipation rate ϵ -equations are assembled and solved respectively.

(step 6) The values of k and ϵ are used to calculate eddy viscosity and hence the diffusivities in the finite volume coefficients.

(step 7) The residual norms are calculated for all conservation equations and normalized by appropriate reference quantities. The convergence criterion is checked, and based upon the result, the algorithm returns to (step 1), using new values of the dependent variables, or the iteration process is terminated.

(3.3) Code Modification for Oscillating Flow

To solve all objectives in this work, the following major changes have been made to the original C.A.S.T computer program.

■ The Lam-Bremhorst version of the low Reynolds number k - ϵ turbulence model was implemented in order to improve fluid flow and heat transfer calculations in the near-wall region. Accordingly, changes in the formulation of the boundary conditions (in particular the wall boundary), and appropriate damping functions used in the k - ϵ equations, are made.

■ The oscillatory flow has a very complicated structure, especially in the Stirling system, where continuous change from laminar to transition and to

turbulent type flows occurs. At the beginning of a cycle, in the whole tube the fluid can be described as laminar. Later, when the acceleration of the fluid is taking place, a turbulent slug forms and advances in the flow direction. The fluid in the tube can still be described as laminar in the portion of the tube where the turbulent slug did not arrive, and turbulent in the region through which the slug has passed. The flow is presumed to be turbulent when the leading edge of the slug arrives at a given axial location within the tube. The empirical transition model used to determine the slug position will be describe in Chapter VI.

- To insure laminar flow in the portion of the tube where the slug has not yet arrived, the turbulent viscosity, which is a part of the effective viscosity, was suppressed (set to zero).

- The original C.A.S.T. code (Peric and Scheuerer (1989)), was designed to solve steady and unsteady problems. Actually the unsteady case was solved by dividing the time domain into a number of time steps (steady cases), where the boundary conditions are varied with time and the solution from one step is an initial guess for the following one. Regarding the oscillation, the acceleration and deceleration of the fluid is accounted for by specifying inflow axial velocity (see equation (2.17)). The inflow and outflow boundary planes are switched every 180° , so the mean velocity from one compile cycle is zero.

CHAPTER IV

Turbulence Modeling of Oscillatory Flow

Since the early seventies, a number of $k-\epsilon$ models have been developed and implemented into various engineering applications. In all of these models, the eddy viscosity concept is used along with two additional partial differential equations which are derived by manipulating the Navier-Stokes equations. These are the transport equations for the turbulence energy (k -equation), and the isotropic turbulence dissipation rate (ϵ -equation).

(4.1) Comparison of Various Turbulence Models

The set of model equations recommended by Launder and Spalding (1972) for high Reynolds number flows have been most widely employed. For the wall bounded flows these equations are used in conjunction with the empirical wall function formulations. The wall functions translate the wall boundary conditions into the region

within $Y^+ = 50$ distance from the wall. Jones and Lauder (1974) extended the $k-\epsilon$ model to low Reynolds numbers, and performed computations right to the wall. Later, other forms of the $k-\epsilon$ model were developed using the same set of k and ϵ equations, but different formulations of the damping functions were used for correct calculation in the near-wall region.

Patel, Rodi and Scheurer (1985) tested and compared eight low Reynolds number turbulence models based on the eddy viscosity concept. Among those models was the Lam-Bremhorst model. They wrote: "... the Lam- Bremhorst $k-\epsilon$ model, ... yields comparable results and performs considerably better than other [models]. However, even this need further refinement if they are to be used with confidence to calculate near wall and low Reynolds number flow...".

A similar comparison was made by Lang and Shih (1991). They tested nine different models. They did not find the Lam-Bremhorst model performance as good as Patel et al. (1985). However, this comparison was made for models with improved damping functions formulations. They found that the Lam-Bremhorst model performed well near and away from the wall. They wrote that "...The standard $k-\epsilon$ model has been proven to provide good results in the high Reynolds number range. It is therefore attractive for a near wall $k-\epsilon$ turbulence model to approach the standard $k-\epsilon$ model away from the wall. The Lam-Bremhorst model is the only $k-\epsilon$ model in this study which possess this characteristic. ... Because the boundary layer and channel flows are self-similar, the solution should be independent of the initial conditions. However, some

of the models [...and Lam-Bremhorst] have difficulty when the initial conditions contain large gradients. ..."

On the basis of these tests, the simplicity of the model, and the successful application to the turbulent oscillatory flow problem, Koehler (1990), the Lam-Bremhorst model was chosen for present study.

(4.2) The Lam-Bremhorst k - ϵ Model

All of the different forms of k - ϵ models based on the eddy viscosity concept use the same form of equations for k and ϵ . The terms of these equations are presented in table II.

Rate of Change	Convection	Diffusion	Generation	Destruction
$\rho \frac{\partial k}{\partial t}$	$+\rho U \frac{\partial k}{\partial x} + \rho V \frac{\partial k}{\partial r}$	$= \frac{\partial}{\partial x} \left(\left(\mu + \frac{\mu_t}{\sigma_k} \right) \frac{\partial k}{\partial x} \right) + \frac{1}{r} \frac{\partial}{\partial r} \left(\left(\mu + \frac{\mu_t}{\sigma_k} \right) \frac{\partial k}{\partial r} \right)$	$+\rho G$	$-\rho \epsilon$
$\rho \frac{\partial \epsilon}{\partial t}$	$+\rho U \frac{\partial \epsilon}{\partial x} + \rho V \frac{\partial \epsilon}{\partial r}$	$= \frac{\partial}{\partial x} \left(\left(\mu + \frac{\mu_t}{\sigma_\epsilon} \right) \frac{\partial \epsilon}{\partial x} \right) + \frac{1}{r} \frac{\partial}{\partial r} \left(\left(\mu + \frac{\mu_t}{\sigma_\epsilon} \right) \frac{\partial \epsilon}{\partial r} \right)$	$+c_1 f_1 \rho G \frac{\epsilon}{k}$	$-c_2 f_2 \rho \frac{\epsilon^2}{k}$

Table II. Terms of the k and ϵ equations.

The turbulent viscosity is modeled, using Prandtl Komogorov's expression as:

$$\mu_T = \rho c_\mu f_\mu \frac{k^2}{\epsilon} \quad (4.1)$$

In the wall bounded flows, the viscous effects become important in the near wall region. Therefore, in the equation (4.1), and in the generation and the destruction terms of the ϵ -equation, the damping functions are introduced.

(4.2.1) The Damping Functions in the Lam-Bremhorst $k-\epsilon$ Model

In the high Reynolds number $k-\epsilon$ model, where the law-of-the-wall is used to define the wall boundary conditions, the damping functions f_μ , f_1 and f_2 are all assumed to be unity. It has been found that this assumption cannot be valid within a laminar sublayer and therefore appropriate functions must be chosen to ensure satisfactory predictions consistent with physical arguments.

□ Function f_μ

Lam and Bremhorst proposed the following expression for f_μ

$$f_\mu = (1 - \exp(-0.0165R_y))^2 \left(1 + \frac{20.5}{R_t}\right) \quad (4.3)$$

where f_μ is a function of R_y and R_t . The presence of the wall has a direct (R_y) and indirect (R_t) influence on f_μ . Numerous applications of the high Re number

model with wall function formulas, suggest that f_μ should approximately be equal to unity in the fully turbulent region remote from the solid walls. This is also consistent with the usual understanding of turbulence, that properties should be fairly uniform in regions where viscous effects are small compared to turbulent ones. On the other hand in regions very near a wall where viscous effects become important properties will change rapidly and f_μ will also differ considerably from unity.

□ Function f_1

Computations with the high Re number form of the model with wall function formulas suggest that f_1 is approximately unity remote from the wall. In the near wall region it is founded that f_1 assumes larger values in order to increase the predicted dissipation rate, thereby reducing the predicted turbulence level to match available experimental data. Lam and Bremhorst proposed that:

$$f_1 = 1 + \left(\frac{0.05}{f_\mu} \right)^3 \quad (4.4)$$

where f_1 is a function of f_μ only, with constants obtained by computer optimization. Close to the wall, f_μ will be small but finite, and f_1 will become large. Away from the wall the turbulence level and f_μ are high. Hence, f_1 will be approximately equal unity.

□ Function f_2

Since (ϵ) and its derivatives $(\partial\epsilon/\partial r)$ and $(\partial^2\epsilon/\partial r^2)$ are not infinite at the wall, (f_2) must tend to zero as R_t tends to zero. Therefore, the proposed formulation for the f_2 function is:

$$f_2 = 1 - \exp(-R_t^2)$$

(4.5)

The expressions for all damping functions used in the Lam-Bremhorst model are listed in table III. Figure 4.1 shows the values of damping functions vs dimensionless distance from the wall, in the turbulent pipe flow problem.

Damping Function	High Re Number Model	Low Re Number Model
f_μ	$f_\mu = 1.0$	$f_\mu = (1 - \exp(-0.0165 R_t))^2 (1 + \frac{20.0}{R_t})$
f_1	$f_1 = 1.0$	$f_1 = 1 + (\frac{0.055}{f_\mu})^3$
f_2	$f_2 = 1.0$	$f_2 = 1 - \exp(-R_t^2)$

Table III. The damping functions in turbulence modeling.

For more detailed information about the model described above, refer to Lam and Bremhorst (1981).

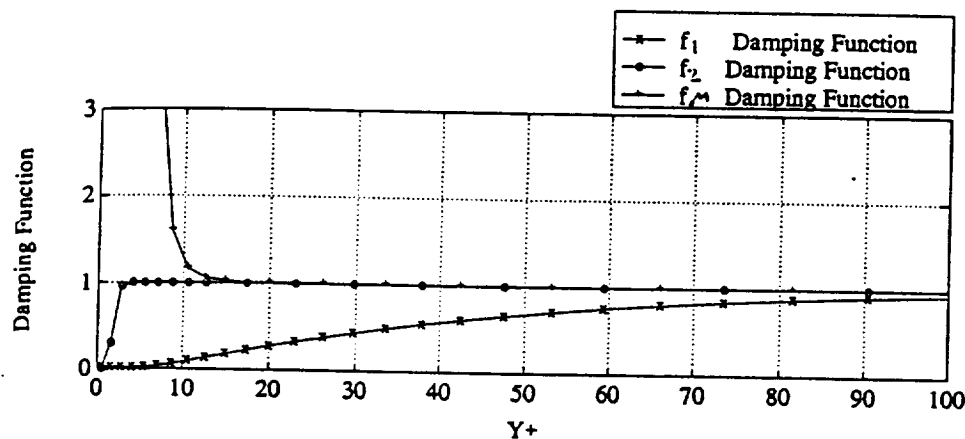


Figure 4.1. The damping functions in the Lam Bremhorst model.

(4.2.2) The Boundary Conditions in the k - ϵ Model

The high Reynolds number model is a special case of the low Reynolds number model, where all damping functions are set to unity. The real difference between the high Reynolds number and the low Reynolds number models is due to the boundary conditions. The boundary conditions are presented in table IV.

Because in some low Reynolds number models the wall values of k and ϵ are defined differently, the additional terms appear in the turbulent transport equations. The Lam Bremhorst model offers the advantage that there are no additional terms. It makes this model easy to implement on base which is C.A.S.T. code, where the high Reynolds number model was originally used.

Boundary Condition	High Re Number Model	Low Re Number Model
@ inlet plane	$\epsilon = 1/(Re^{0.5}) \rho \frac{k^2}{\mu}$ $k = (3/2)(TI U_{max})^2$	$\epsilon = (1/11 Re^{0.875}) \rho \frac{k^2}{\mu}$ $k = (3/2)(TI U_{max})^2$
@ outlet plane	$\frac{\partial k}{\partial x} = \frac{\partial \epsilon}{\partial x} = 0$	$\frac{\partial k}{\partial x} = \frac{\partial \epsilon}{\partial x} = 0$
@ wall	$\epsilon = U_*^3 / \kappa y, \quad \frac{\partial k}{\partial r} = 0$	$\epsilon = \nu \frac{\partial^2 k}{\partial y^2}, \quad k = 0$
@ center line	$\frac{\partial k}{\partial r} = \frac{\partial \epsilon}{\partial r} = 0$	$\frac{\partial k}{\partial r} = \frac{\partial \epsilon}{\partial r} = 0$

Table IV. Boundary Condition for the high Reynolds number and the low Reynolds number models.

(4.3) Evaluation of the Constants in the $k-\epsilon$ Model

There are five empirical constants used in the $k-\epsilon$ turbulence modeling.

- c_μ was determined from experiments in thin shear layers using the relation:

$$c_\mu = \left(\frac{\overline{U'V'}}{k} \right)^2 \quad (4.6)$$

The value in the above equation was measured by Champagne, Harris and

Corrsin (1970) as $c_\mu = 0.09$.

- c_2 was found studying isotropic turbulence for high Re number flows. Batchelor

and Townsend (1948) found that for grid generated turbulence at high Reynolds numbers, k is inversely proportional to the distance to the grid $k \sim 1/x$. From calculation $c_2 = 2$, which was later adjusted to 1.92.

- c_1 can be determined from the ϵ transport equation, using the law of the wall and the assumption that near wall shear stress is approximately equal to the wall shear stress. c_1 can be expressed in the formulation:

$$c_1 = c_2 - \frac{\kappa^2}{\sigma_\epsilon \sqrt{c_\mu}} \quad (4.7)$$

to which the ϵ equation reduces in zero pressure gradient local equilibrium flows with a logarithmic velocity distribution. For $c_2 = 1.92$, $\kappa = 0.4$, $\sigma_\epsilon = 1.3$ the value is $c_1 = 1.44$.

- σ_k and σ_ϵ have a meaning as turbulent Prandtl numbers which were founded by computer optimization.

The values of all constants used in this work are listed in table V.

c_μ	0.09
c_1	1.44
c_2	1.92
σ_k	1.0
σ_ϵ	1.3

Table V. Turbulent modeling constants.

ORIGINAL PAGE IS
OF POOR QUALITY

(4.4) The Empirical Transition Model

Based on the experimental data obtained at the University of Minnesota, (see Seume et. al. (1992)), an empirical transition model has been recently developed (Simon et. al. (1992)). In this model a flow is considered turbulent as result of one of the two following mechanisms: (1) boundary layer growth, (2) ingested turbulence slug, whichever occurs earlier in the cycle.

(1) Boundary layer growth:

At the beginning of each half-cycle the core of the fluid accelerates as a slug and a boundary layer grows near the wall. When the boundary layer momentum thickness Reynolds number (Re_{δ_2}) exceeds the critical value, the flow at that position becomes turbulent. Critical values of the momentum thickness Reynolds number are calculated from the following expression presented by Mayle, (1991):

$$Re_{\delta_2, crit} = 400 (TI \%)^{-5/8}$$

where turbulence intensity, TI , can be expressed as:

$$TI \% = \frac{U'_{mean}}{U_{mean}} \times 100$$

where U'_{mean} represents the rms fluctuation velocity averaged over the cross-sectional area of the core, and U_{mean} is the bulk-mean velocity.

(2) Turbulence slug position:

In this mechanism, it is assumed that the flow in the pipe is at low turbulence level and there is an ingested turbulence slug that will travel with the mean flow. At the

arrival of this slug to any axial location, the flow becomes turbulent. The following is used to find an expression for the point in the cycle at which the leading edge of the slug appears at the particular axial position. Using definition:

$$U_{mean}(\theta) = U_{max} \sin(\theta)$$

$$X_{slug}(t) = \int_0^t U_{mean} dt$$

and substituting $\theta = \omega t$, $Re_{max} = U_{max} D/\nu$ and $Va = \omega D^2/4\nu$ gives:

$$X_{slug} = \frac{Re_{max} \nu}{D \omega} \int_0^t \sin(\omega t) dt$$

$$X_{slug} = \frac{Re_{max} \nu}{D \omega} (1 - \cos(\omega t))$$

$$X_{slug}/D = \frac{1}{4} \frac{Re_{max}}{Va} (1 - \cos(\theta))$$

where X_{slug} is an axial slug position.

CHAPTER V

Code Validation with Pipe Flow under Steady State Conditions

In order to verify both turbulence modeling and the computer code, a series of computational tests were made to compare the predictions for pipe flow under steady state conditions. Concerning fluid mechanics, calculations were made at four different inflow velocities to cover laminar, transitional and turbulent flows, using three numerical models. These models are:

- the High Reynolds Number $k-\epsilon$ Model, where the turbulence transport equations are solved along with the wall functions, and the surface boundary conditions are shifted away from the wall to the point in the fluid where the molecular viscosity effect is small;
- the Low Reynolds Number $k-\epsilon$ Model, where the turbulence transport equations are solved, the wall damping effect is modeled, and the direct influence of molecular viscosity is accounted for;
- the Laminar Model, where there is no turbulence modeling and turbulent intensity is assumed to be zero.

These models are used to predict fully developed velocity profiles which are discussed in Section (5.1). Concerning heat transfer, the Nusselt number is computed for fully developed steady flow in a tube with constant wall temperature. These calculations are discussed and compared with analytical solutions in Section (5.2).

(5.1) Fully Developed Flow

All calculations were made assuming steady state flow conditions with a uniform inflow velocity at the inlet plane. To insure the fully developed velocity profile, the computational domain was defined such that $L/D = 120$. For computations with the Low Reynolds Number Model and the Laminar Model, a 62×72 grid was used with uniform grid distribution in the axial direction and nonuniform in radial direction with higher grid density near the wall. For the High Reynolds Number Model, a 62×40 grid was used with uniform grid distribution in both directions.

Laminar flow: $Re = 500$

Figure 5.1 shows the predicted fully developed velocity profiles in dimensionless coordinates for laminar flow with $Re = 500$. As a reference line the universal profile from the Law-of-the-Wall (lower of $U^* = Y^*$, $U^* = 2.44 \ln(Y^*) + 5.5$) is presented (dashed line). For low inflow velocity, $Re = 500$, the flow is laminar. Most of the velocity profile is in the $U^* = Y^*$ region. The Low Reynolds Number Model and the Laminar model predict identical profiles. Both are in excellent agreement with the

universal profile line near the wall, and are shifted away from this line away from the wall, outside the boundary layer where the core velocity is constant. The High Reynolds Number Model is not applicable for such a slow flow and predicts a velocity as much too high. This model was developed for turbulent flows so such a weak agreement can be expected.

Transition flow: $Re = 5000$

Figure 5.2 shows dimensionless velocity profiles for transition flow at $Re = 5000$. The Laminar and the Low Reynolds Number Models show laminar profiles where most of the velocity distribution follows the $U^* = Y^*$ curve. The High Reynolds Number Model predicts turbulent flow where the velocity distribution roughly follows the $U^* = 2.44 \ln(Y^*) + 5.5$ curve. None of the solutions for steady state flow at $Re = 5000$ appear to be satisfactory, as seen in figure 5.2.

Turbulent flow: $Re = 15000$

Figure 5.3 shows velocity profiles in dimensionless coordinates at the inflow velocity corresponding to $Re = 15000$. At this value of the Reynolds number, the flow is turbulent. At this condition, the Laminar Model performance is not good because it predicts a laminar profile according to the relation $U^* = Y^*$ not only in the near wall region, but also throughout the core flow. The High Reynolds Number Model follows the universal profile in the logarithmic region, but and is not correctly predicting the velocities in the viscous region where the wall functions are used. The Low Reynolds Model is seem to match the universal profile very well, and is the only model which

correctly works near and away from the wall.

Highly turbulent flow: $Re = 50000$

Figure 5.4 shows dimensionless velocity profiles for turbulent flow at $Re = 50000$. The comparison between the discussed numerical models is the same as for turbulent flow with $Re = 15000$. As expected, the Laminar Model shows its inapplicability for turbulent flow. The Low Reynolds Model matches the universal profile near the wall, in the buffer zone, and in the logarithmic and the overlap regions. The High Reynolds Model predicts the velocity profile only in the logarithmic and overlap regions.

From the above discussion, one can see that the Laminar Model, where only molecular viscosity is used and no turbulence is modeled, can be used for flows in the laminar and the transition regimes. Only in these regimes, the results are comparable with the more advanced Low Reynolds Model. The High Reynolds Model shows good performance in handling turbulent flows, but yields incorrect results in the laminar cases. Among tested models only Low Reynolds Model shows an ability obtain accurate velocity profiles in steady state laminar, transition, and turbulent flows.

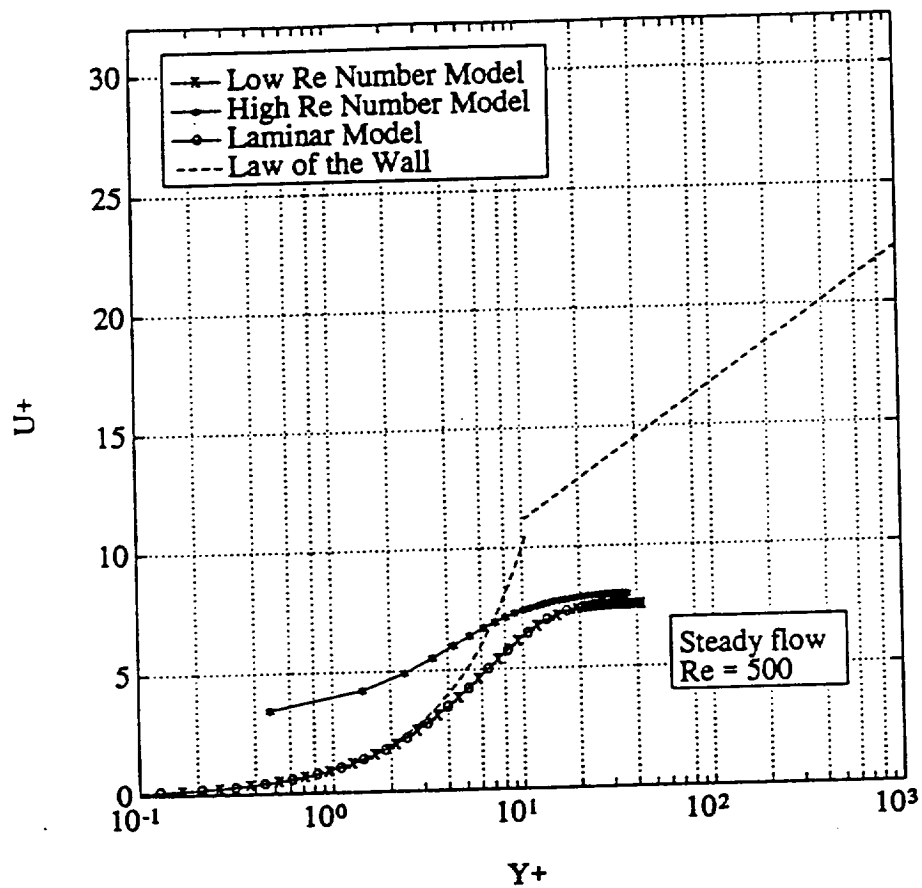


Figure 5.1. Dimensionless velocity profile for the steady state fully developed pipe flow at $Re = 500$.

ORIGINAL
QUALITY

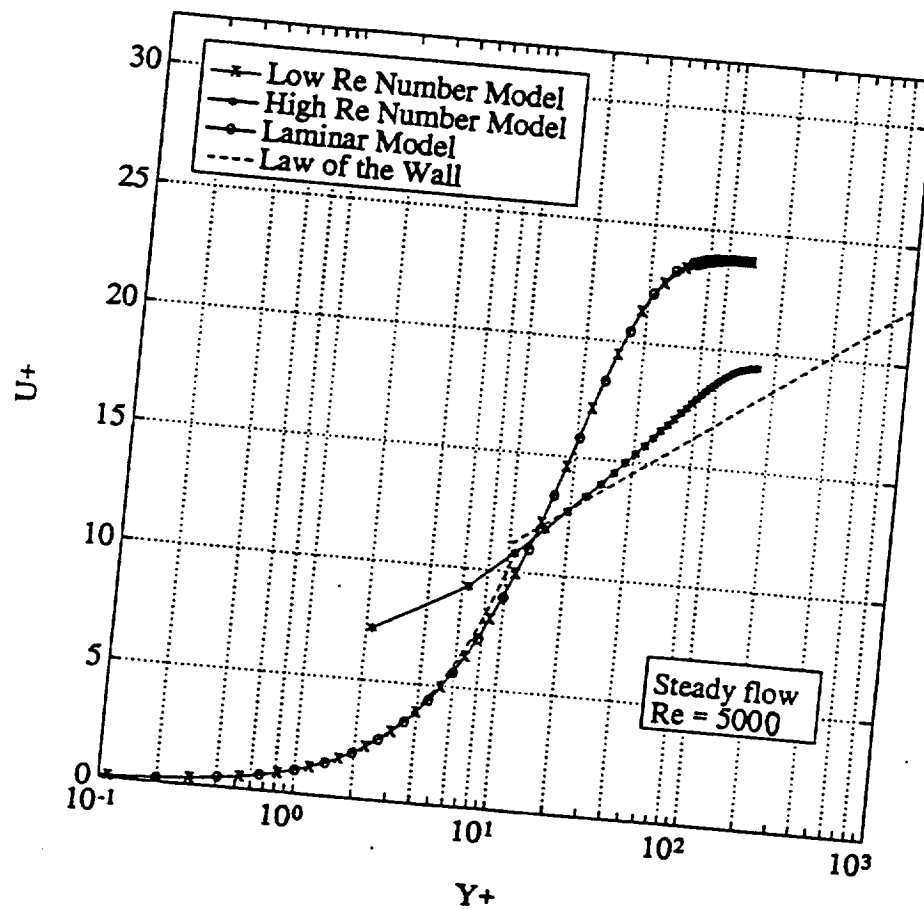


Figure 5.2. Dimensionless velocity profile for the steady state fully developed pipe flow at $Re = 5000$.

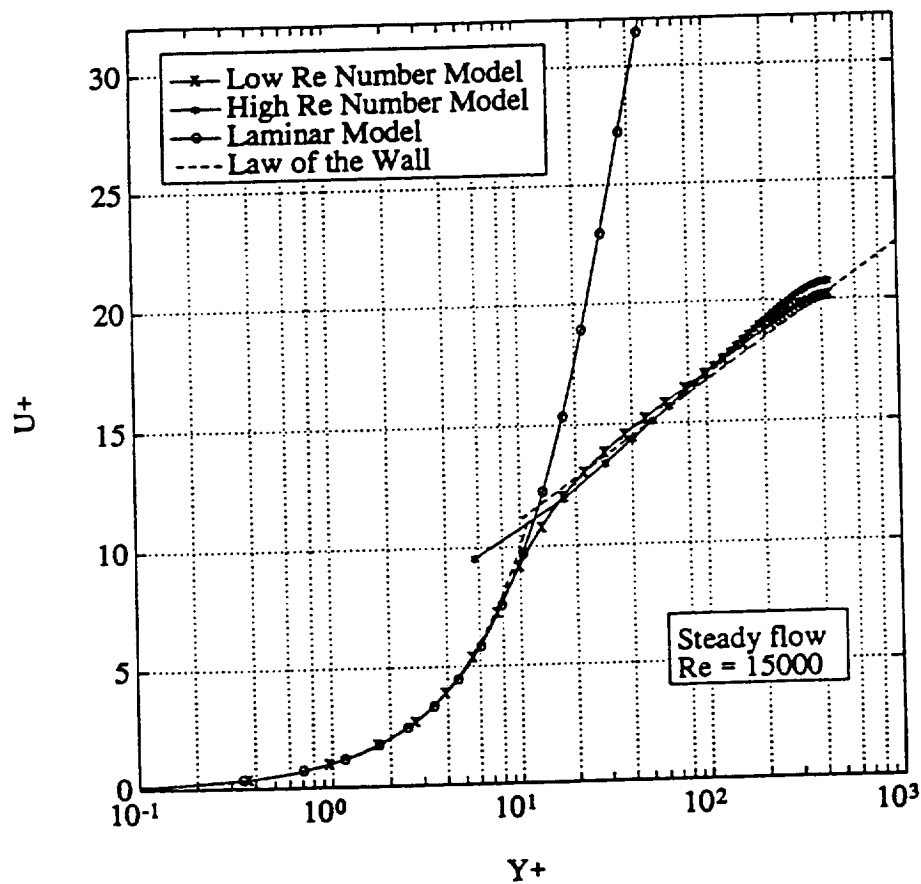


Figure 5.3. Dimensionless velocity profile for the steady state fully developed pipe flow at $Re = 15000$.

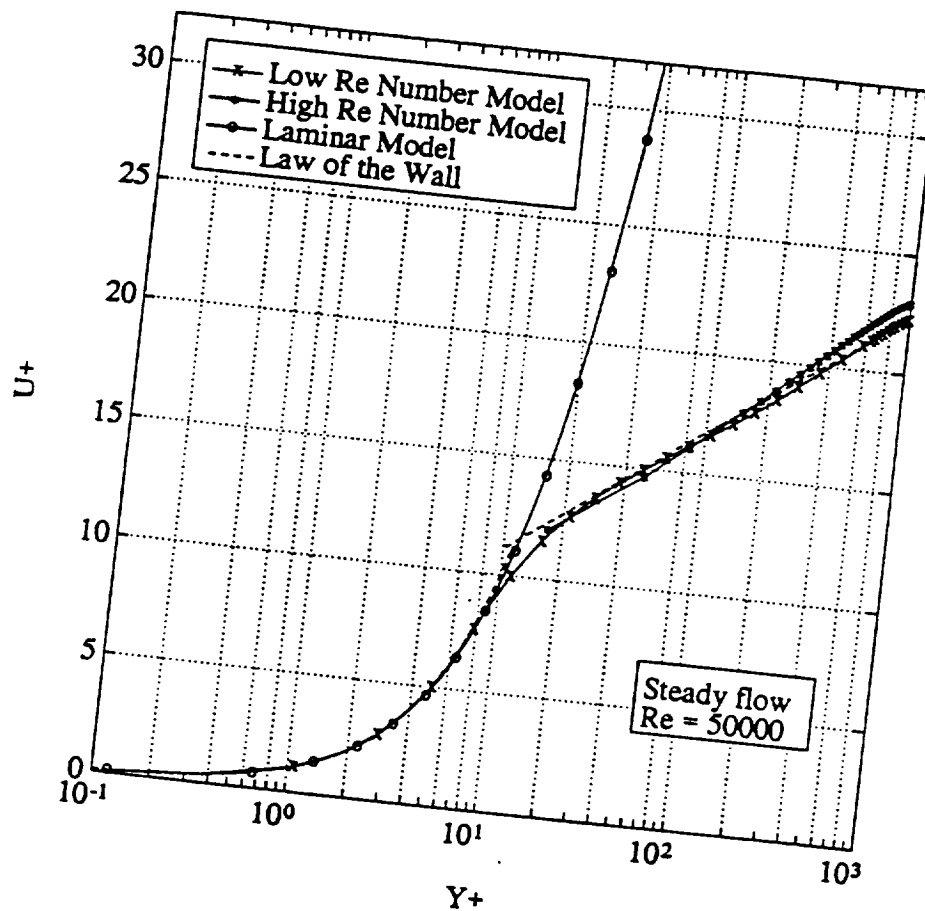


Figure 5.4. Dimensionless velocity profile for the steady state fully developed pipe flow at $Re = 50000$.

(5.2) Heat Transfer

Two models were used to calculate Nusselt numbers for constant-wall-temperature steady-state pipe flow namely : the Laminar Model and the Low Reynolds Model. Because, the thermal entry length is typically greater than the hydrodynamic entry length, a longer tube was chosen with the computational domain of $L/D = 300$. Calculations were made for two cases: the laminar flow with $Re = 500$, and the turbulent flow with $Re = 15000$. Both were compared with the analytical solution for Nusselt number, presented by Kays and Crawford (1993). For laminar flow inside a constant wall temperature tube, the analytical solution is $Nu = 3.658$. For the flow with $Re = 500$, the prediction from the Laminar Model and from the Low Reynolds Model the same, and $Nu = 3.910$. For turbulent flow using the following algebraic empirical equation:

$$Nu = 0.062 Pr^{0.4} Re^{0.7} \quad (5.1)$$

the values of Nusselt number is 45.56. Numerical calculations gives: $Nu = 3.910$ for the Laminar Model and $Nu = 55.902$ for the Low Reynolds Model

For laminar flow, the agreement between the analytical solution and the numerically predicted Nusselt numbers, from the Laminar and the Low Reynolds Models is good, differing only by 6%. For turbulent flow, the Laminar Model gives a very low value for Nusselt number, and is the same as for laminar flow for $Re = 500$. The Low Reynolds Model overpredicts the Nusselt number by 20%, what is accepted since it is known that equation (5.1) has its accuracy in this range.

CHAPTER VI

Numerical Results and Comparison with Experiment

Modeling efforts for turbulent fluid flow and heat transfer can be evaluated by comparing the computational predictions with experimental data. The code validation section (Chapter V) provides the basis of these evaluations and establishes a level of confidence based not only on the computation scheme used but also upon the turbulence model utilized. In this thesis, turbulence modeling assumptions for steady state conditions have been extended to unsteady flow conditions, and particularly oscillatory (with zero mean) flow conditions. In this chapter the numerically predicted solutions are compared with experimental data, obtained from an oscillatory flow apparatus at the University of Minnesota, which now will be briefly described.

(6.1) Description of the Experiment

The experimental facility at the University of Minnesota has been designed to provide both fluid flow and heat transfer data for oscillatory flows. The schematic view of that facility is presented in Figure 6.1.

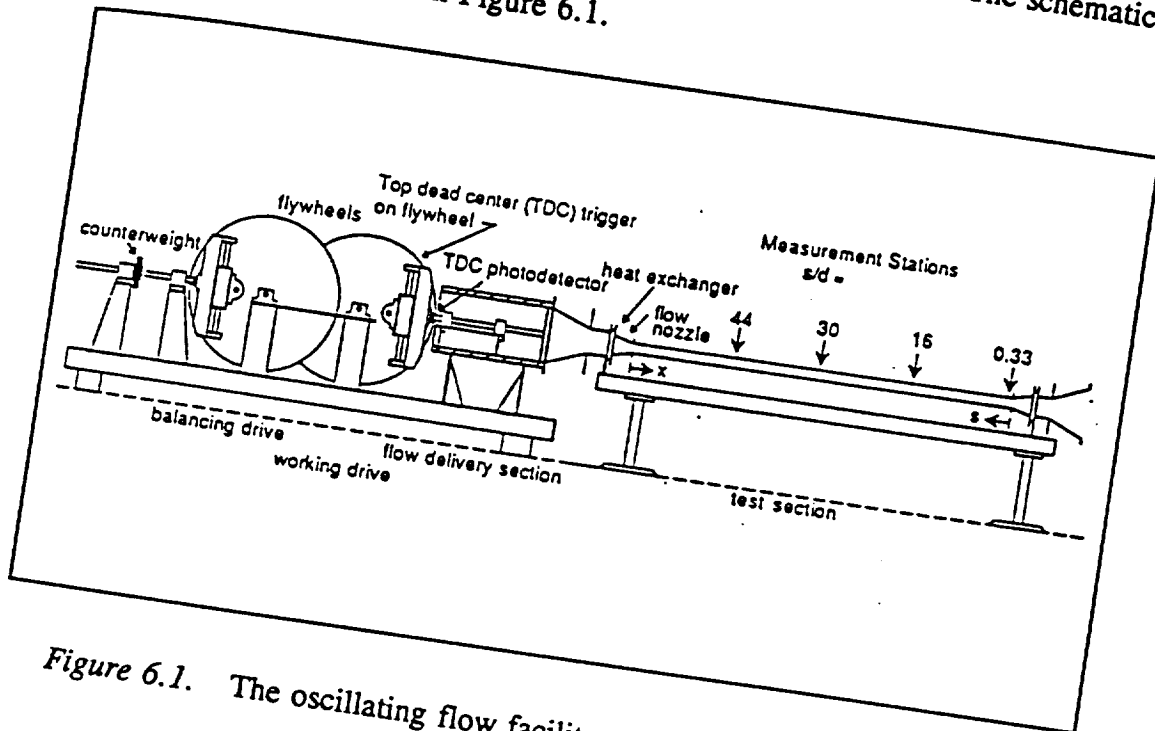


Figure 6.1. The oscillating flow facility at the University of Minnesota.

The test section is a straight tube, with one end connected to the flow delivery section and the other open to the room. The reciprocating piston in the cylinder produces an oscillatory gas flow motion. Both ends of the test tube are connected to smooth nozzles to keep flow from separating upon entry and to make the inflow conditions nearly symmetrical. In some cases, a flush square entry has been used in place of the nozzle. Measurements were taken at various radial positions in four stations located along the test section, and identified as $X/D = 0.33, 16, 30, 44$ respectively (in Figure 6.1). The test was instrumented with a hot-wire anemometer system. Single wire probes were used

to measure the mean velocity, \bar{U} , and the rms fluctuation of the axial component of the velocity, U' . The cross-wire probes were used to add the radial velocity components mean, \bar{V} , and rms-fluctuation, V' , as well as the Reynolds shear stress, $-\overline{U'V'}$. The Top Dead Center (TDC) a photodetector was used to detect the position of the piston, so that the hot wire measurements could be related to a certain crank angle. Typically the measurements taken were an ensemble average of the measurements obtained over 500 cycles or more.

The experiment was designed and operated to simulate the SPDE Stirling engine heater performance in terms of three dimensionless parameters, the maximum tube Reynolds number of the cycle (Re_{max}), dimensionless frequency of oscillation (Valensi number Va), and mean fluid displacement rates (A_r). Air at room temperature was used as a working fluid. The operating parameters of the experiment are listed in table VI.

Re_{max}	11840
Va	80.2
A_r	1.22
D [m]	0.038
L/D	60

Table VI. The operating parameters.

For a more detailed description of the experiment and for all the experimental data refer to Seume et al. (1992).

(6.2) Fluid Flow Predictions

Three numerical models were used to predict the fluid flow:

- THE LAMINAR MODEL, where the flow is assumed to be laminar everywhere, so no turbulence modeling is needed. In the numerical code the value of turbulent viscosity was set to zero ($\mu_T = 0$).
- THE TURBULENT MODEL, where turbulence is modeled utilizing the Lam-Bremhorst version of a low Reynolds number $k-\epsilon$ turbulence model. In this model the $k-\epsilon$ is kept active throughout the cycle and at all axial locations.
- THE TRANSITION MODEL, where an empirical transition model has been utilized to activate the $k-\epsilon$ model at different times of the cycle and axial locations in the tube.

In the computation a 60 (axial) by 70 (radial, half of the pipe) grid was used for all unsteady cases, with the grid density being high near the wall and sparse away from it in the transverse direction, and a uniform grid density in the axial direction. The convergence criterion was set as a 0.1% of the global residual norms for every dependent variable. For each case 120 time steps per cycle were used. In most cases the steady oscillating flow conditions, when there is no cycle-to-cycle variation, were reached after three to four cycles. Under laminar flow conditions throughout the cycle (not the focus of this study - see Ahn and Ibrahim (1992)) the comparison between experiment and computation should be done using the steady oscillating flow results, i.e. in the fourth

cycle or more. However, if transition to turbulence takes place in the cycle, enough mixing will be generated in the first half cycle and based on experimental observations, the second half of the cycle is isolated from the first half. Therefore, it is appropriate to compare the experiment with the first half-cycle computational results.

(6.2.1) Velocity Profiles

Normalized Velocity Profiles.

Figure 6.2b shows the computed radial velocity profiles normalized using the center line velocities at the axial location $X/D = 30$, (midplane), for different crank angles during the cycle. Two numerical models, the Laminar and the Transition models, are compared with the experimental data. At the crank angle $\theta = 30^\circ$, and $\theta = 60^\circ$, when flow is expected to be laminar, both models show the same profiles and are in good agreement with the experimental data. Later, at $\theta = 90^\circ$, the flow is turbulent, and as one could expect, the Transition Model is in excellent agreement with experimental data near the wall, and is in good agreement with this data away from the wall. Similar agreement is at higher crank angle positions $\theta = 120^\circ$, $\theta = 150^\circ$, and $\theta = 170^\circ$, the flow is decelerating and relaminarization might occur, (not very good agreement at $\theta = 150^\circ$). The Laminar Model predictions, as expected, are completely different from the experimental data at higher crank angles (e.g. $\theta = 170^\circ$), where the flow reversal near the wall takes place. Figure 6.2a shows similar plots to Figure 6.2b at $X/D = 16$. For all crank angle positions the agreement between the Transition Model and the

experiment is good, except the location of relaminarization. The Laminar Model predictions, are good at locations for $\theta \leq 150^\circ$, but different from the experimental data at crank angles $\theta = 170^\circ$, where the flow reversal near the wall takes place. Figure 6.2c shows similar plots to Figure 6.2b at $X/D = 44$. The agreement between the experimental data and the computational results are similar to what was described in Figure 6.2b.

Comparing Figures 6.2a,b,c one can see that excellent agreement between the experimental data and the computations in the laminar portion of the cycle takes place. The occurrence of transition is located accurately by the Transition Model. More over, the agreement between the experiment and computations in the turbulent portion of the cycle is good, and gets better at higher X/D values.

Dimensionless Velocity Profiles (U^+ vs Y^+)

Figures 6.3a,b,c show the dimensionless velocity U^+ vs dimensionless distance from the wall Y^+ on a semi logarithmic scale for selected crank angles at $X/D = 16, 30$, and 44. This form of data presentation allows looking at the velocity near the wall in the viscous sublayer region. On the plots, the universal velocity profile from the Law of the Wall ($U^+ = Y^+$, $U^+ = 2.44 \ln Y^+ + 5.5$) is presented (dashed line). Comparison between the experimental data and the Transition Model predictions is summarized in Table VII.

Location in the Tube	Crank Angle	Flow Type from Experiment	Computational Agreement with Experiment
X/D=16 X/D=30 X/D=44	30	laminar laminar laminar	excellent excellent excellent
X/D=16 X/D=30 X/D=44	60	laminar laminar laminar	good good good
X/D=16 X/D=30 X/D=44	90	turbulent turbulent laminar	excellent very good good
X/D=16 X/D=30 X/D=44	120	laminar turbulent turbulent	fair very good very good
X/D=16 X/D=30 X/D=44	150	laminar turbulent turbulent	fair good excellent
X/D=44	170	turbulent	fair

Table VII. Evaluation of Figures 6.3a,b,c.
Scale: excellent $\pm 5\%$, very good $\pm 10\%$, good $\pm 25\%$, fair $> \pm 50\%$.

Figures 6.3a,b,c provide another way of comparing the experimental data with the computations. In these figures the near-wall region is expanded and friction velocity is used in the normalization of both velocity and distance. Similar conclusions to these from Figures 6.2a,b,c are noticed. Again the Transition Model is capable of predicting the laminar and turbulent parts of the cycle accurately. The only difficulty is for high angles (near $\theta = 170^\circ$ and above for $X/D = 30, 44$, and $\theta = 120^\circ$ and above for $X/D = 16$) where the flow decelerates and relaminarization might occur.

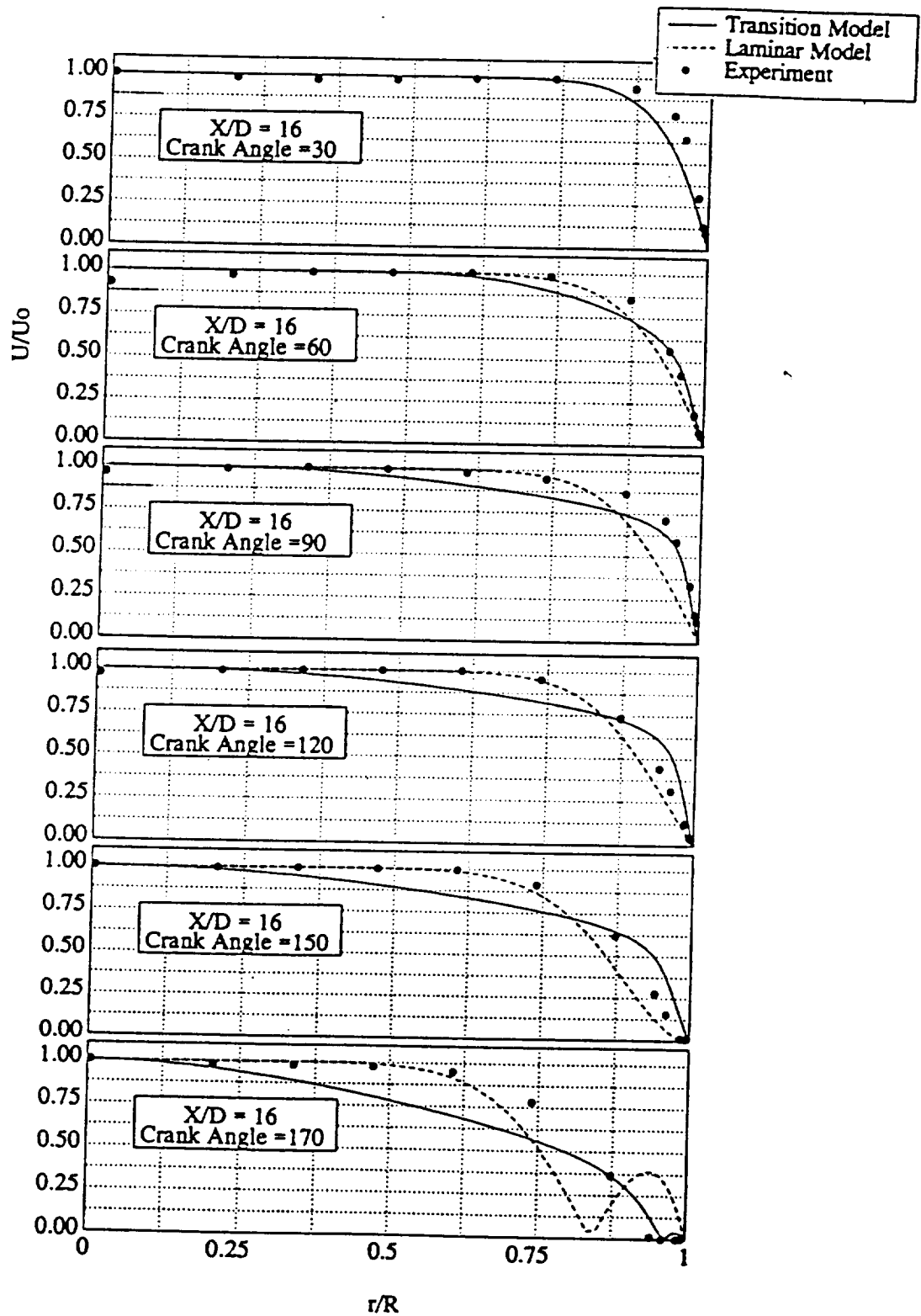


Figure 6.2a. Normalized velocity profile for oscillatory pipe flow at $X/D = 16$.

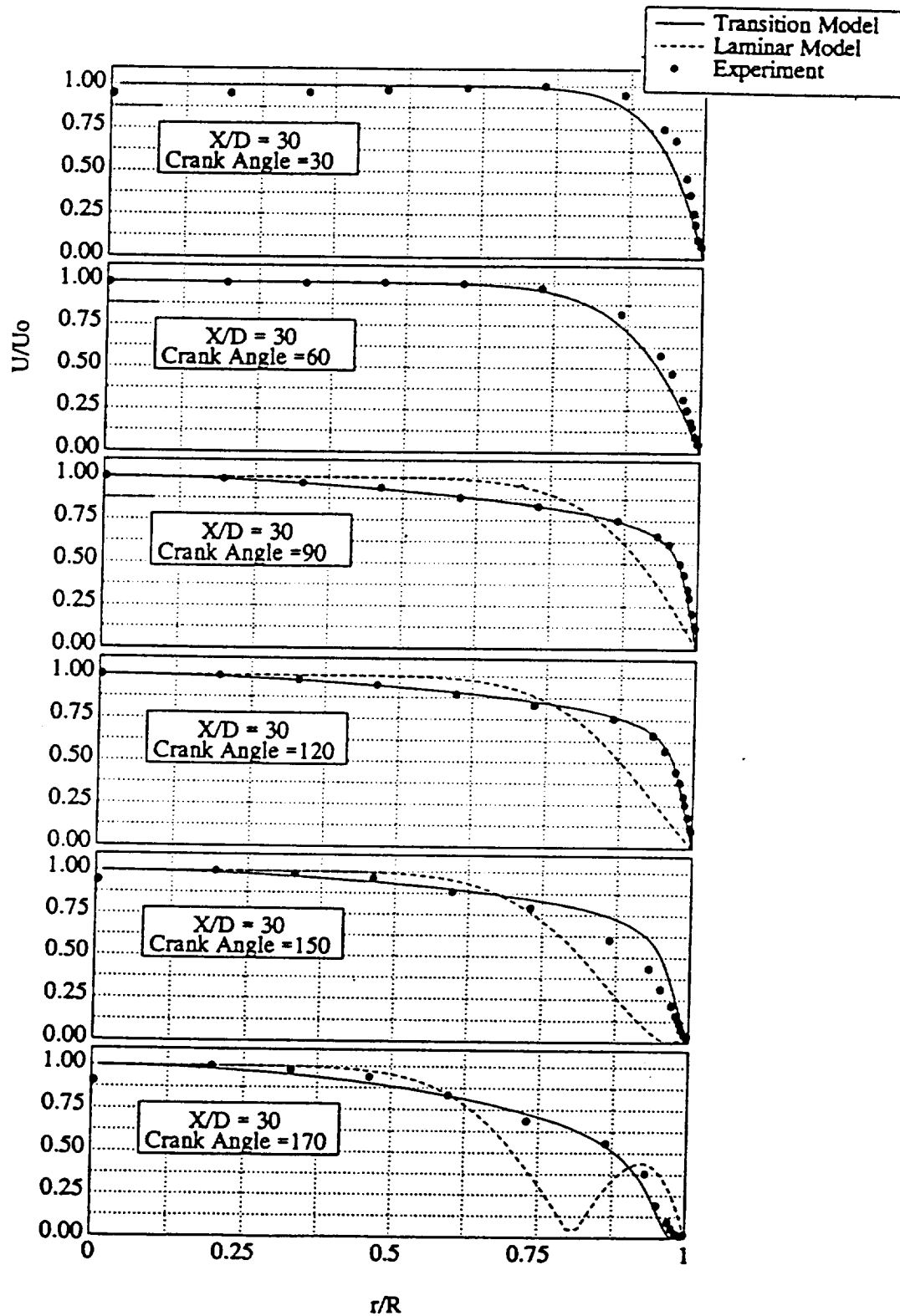


Figure 6.2b. Normalized velocity profile for oscillatory pipe flow at $X/D = 30$.

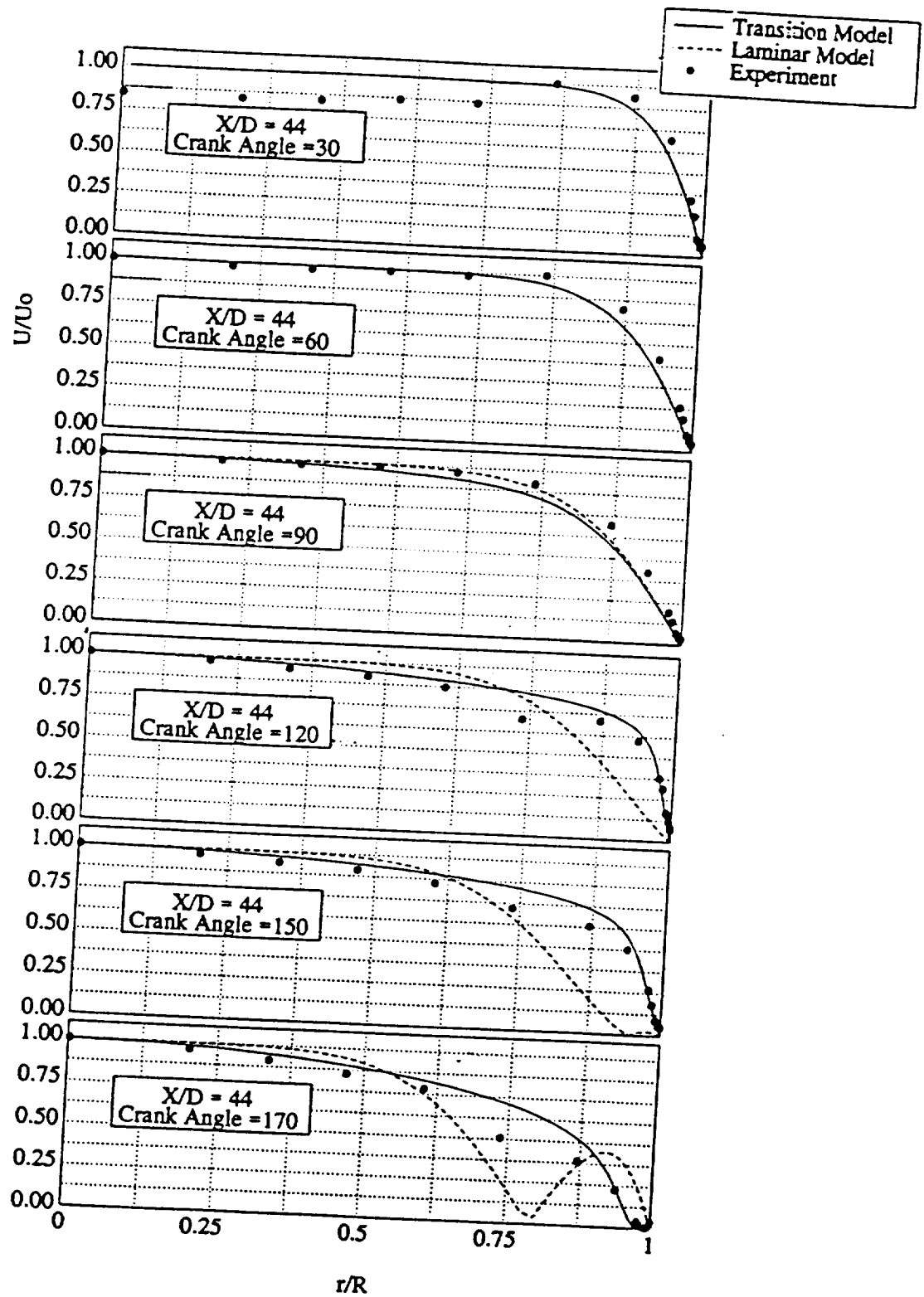


Figure 6.2c. Normalized velocity profile for oscillatory pipe flow at $X/D = 44$.

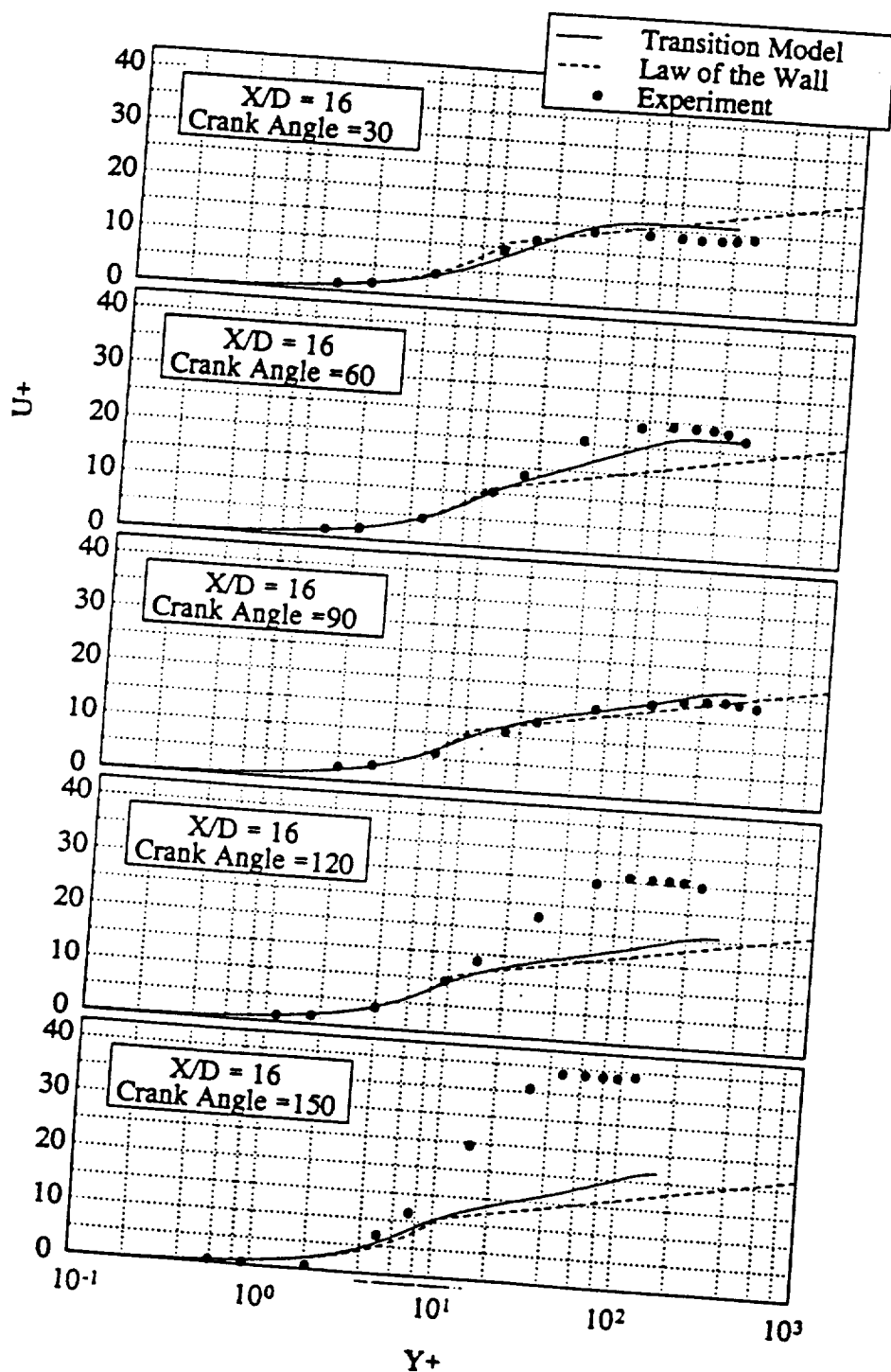


Figure 6.3a. Dimensionless velocity (U^+) profile for oscillatory pipe flow at $X/D = 16$.

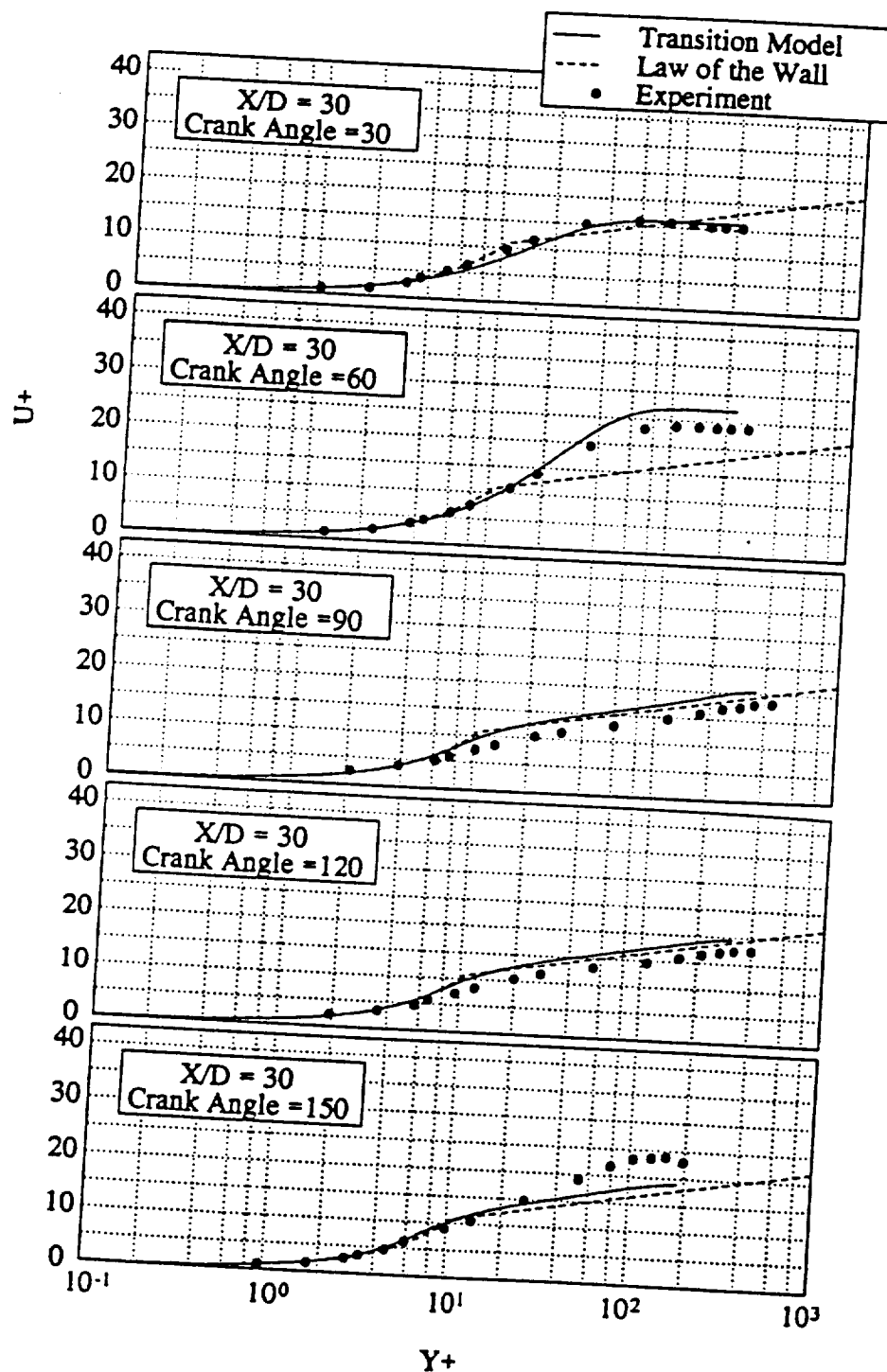


Figure 6.3b. Dimensionless velocity (U^+) profile for oscillatory pipe flow at $X/D = 30$.

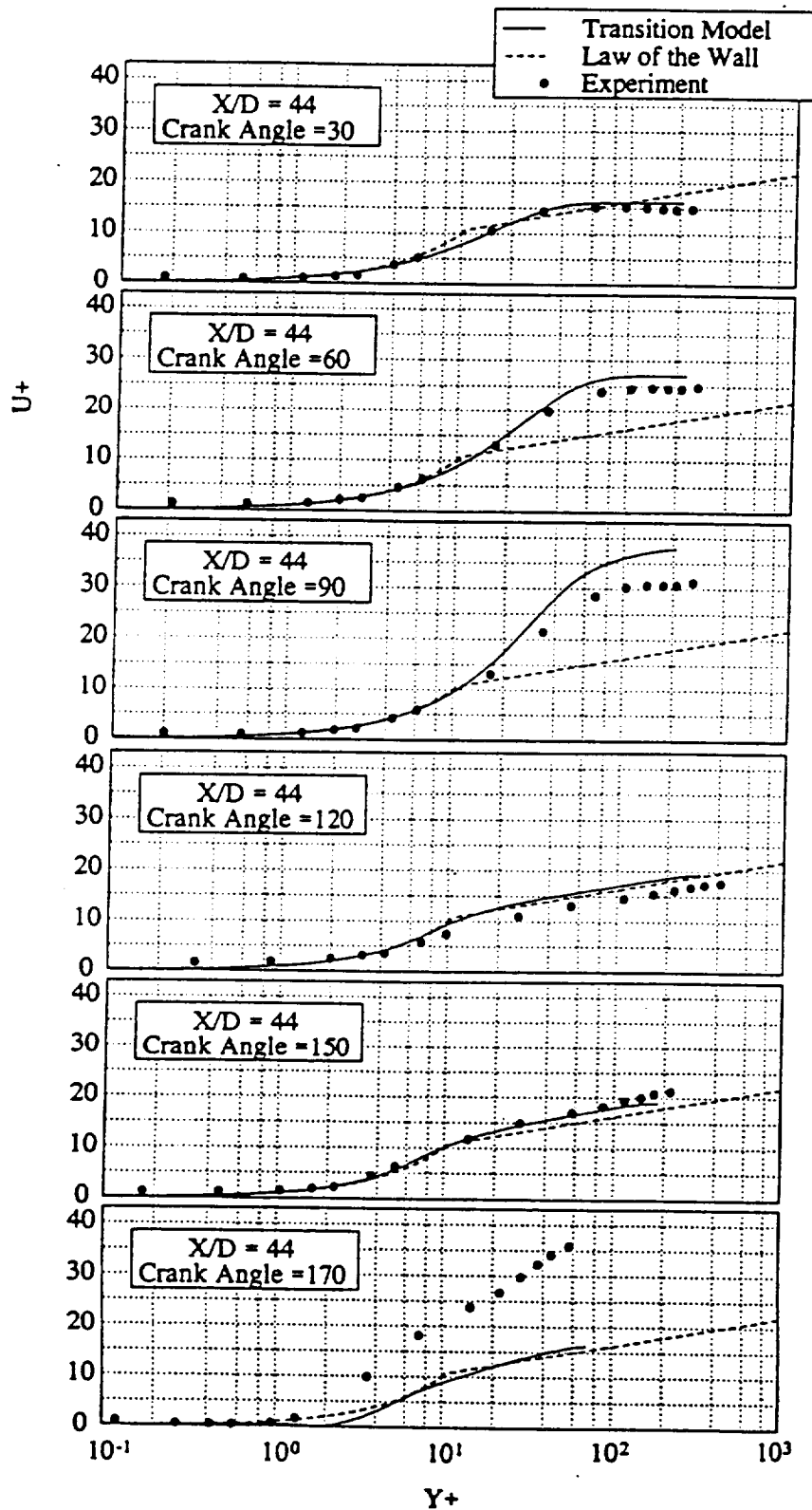


Figure 6.3c. Dimensionless velocity (U^+) profile for oscillatory pipe flow at $X/D = 44$.

(6.2.2) Turbulent Kinetic Energy

In the k - ϵ turbulence modeling, the transport equation for the turbulent kinetic energy (equation 2.7), is a basis for describing the transport processes in fluid motion. The turbulent kinetic energy is defined as:

$$k = (1/2) \overline{(U'^2 + V'^2 + W'^2)} \quad (6.1)$$

In the experiment, where the hot-wire anemometer was used, the fluctuating components of the velocity (U' and V') were measured. In order to obtain k , one should make an assumption about W' . In this study, $W' = V'$, which is appropriate in the turbulent core where turbulence is actually isotropic.

$$k = (1/2) \overline{(U'^2 + 2V'^2)} \quad (6.2)$$

Figure 6.4a illustrates the comparison between numerical and experimental predictions for turbulent kinetic energy vs distance from the wall for different crank angles at the axial location $X/D = 16$. In the laminar portion of the cycle, at $\theta = 30^\circ$, the computed values of k , as well as experimental data, are close to zero. Later, when a turbulent slug is advancing into the tube, the values of k increase. The highest values of k are obtained at about $\theta = 90^\circ$, where the agreement with the experimental results is the best. At this crank angle, the flow is turbulent. The calculated value of k rises quickly from zero at the wall, up to a maximum near the wall, and gradually decreases to its lowest values at the center-line of the tube. For larger crank angles, the

experimental results show a decrease in the value of k , as a result of the flow deceleration and possible relaminarization. Figures 6.4b and 6.4c show plots similar to those in Figure 6.4a but for $X/D = 30$ and 44 respectively. At $X/D = 30$ and 44 good agreement between predictions and experiment are noted at almost all crank angles for the value of k . It should be noted that the profiles shown on Figure 6.4b are for $\theta \geq 60^\circ$, the slug arrives at about $\theta = 75^\circ$, after which the flow become turbulent. Similarly, on Figure 6.4c only profiles for $\theta \geq 90^\circ$ are shown since the slug arrives at about $\theta = 105^\circ$.

(6.2.3) Skin Friction Factor

Figure 6.5 shows the Transition Model prediction of the friction coefficient as it varies through the first half cycle at three locations of the tube, $X/D = 16, 30, 44$. Also on the figure, the experimental data, the results from the Laminar Model and the Turbulent Model are shown. The friction coefficient, C_f , is defined as:

$$C_f = \frac{\tau_w}{(1/2)\rho U_i^2} = 2\left(\frac{U^*}{U_i}\right)^2 \quad (6.3)$$

where U_i is the average instantaneous velocity across the cross section of the channel. Since at the crank angles $\theta = 0^\circ, 180^\circ$ the average instantaneous velocity values are almost zero, and the friction coefficient approaches infinity. In the laminar portion of the cycle, the Laminar Model predictions are in excellent agreement with the experimental

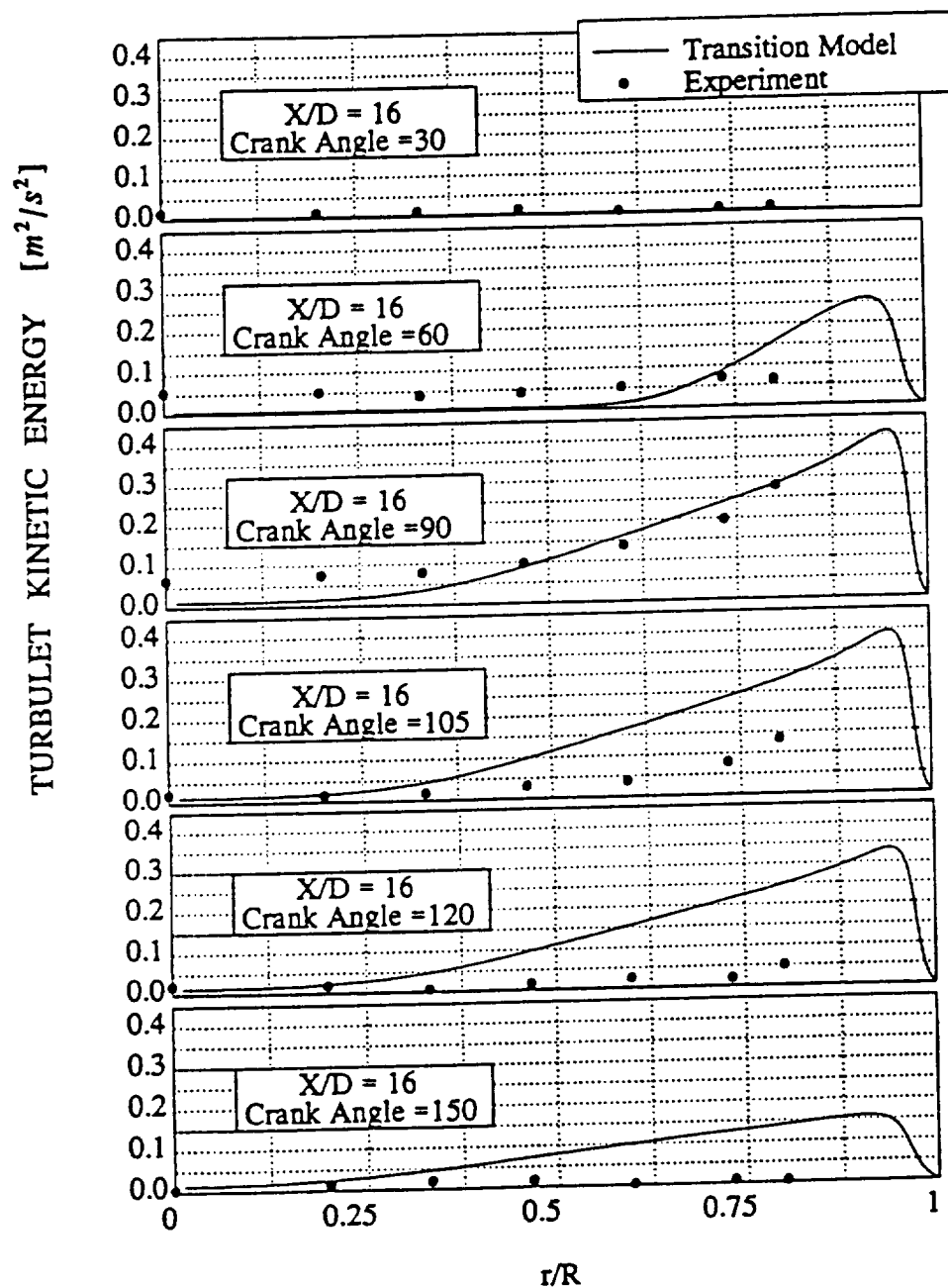


Figure 6.4a. Turbulent kinetic energy (k) profile for oscillatory pipe flow at $X/D = 16$.

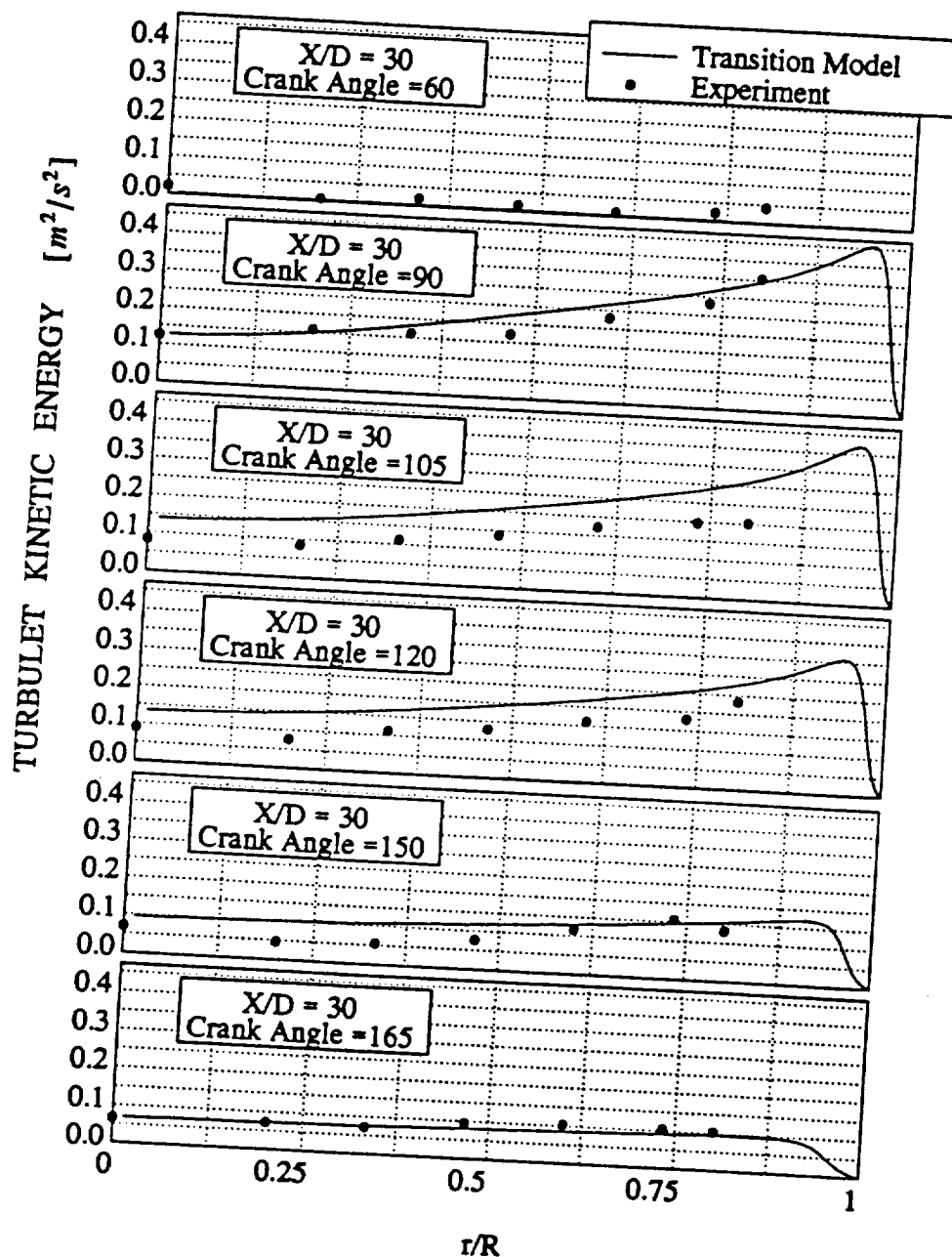


Figure 6.4b. Turbulent kinetic energy (k) profile for oscillatory pipe flow at $X/D = 30$.

ORIGINAL PAGE IS
OF POOR QUALITY

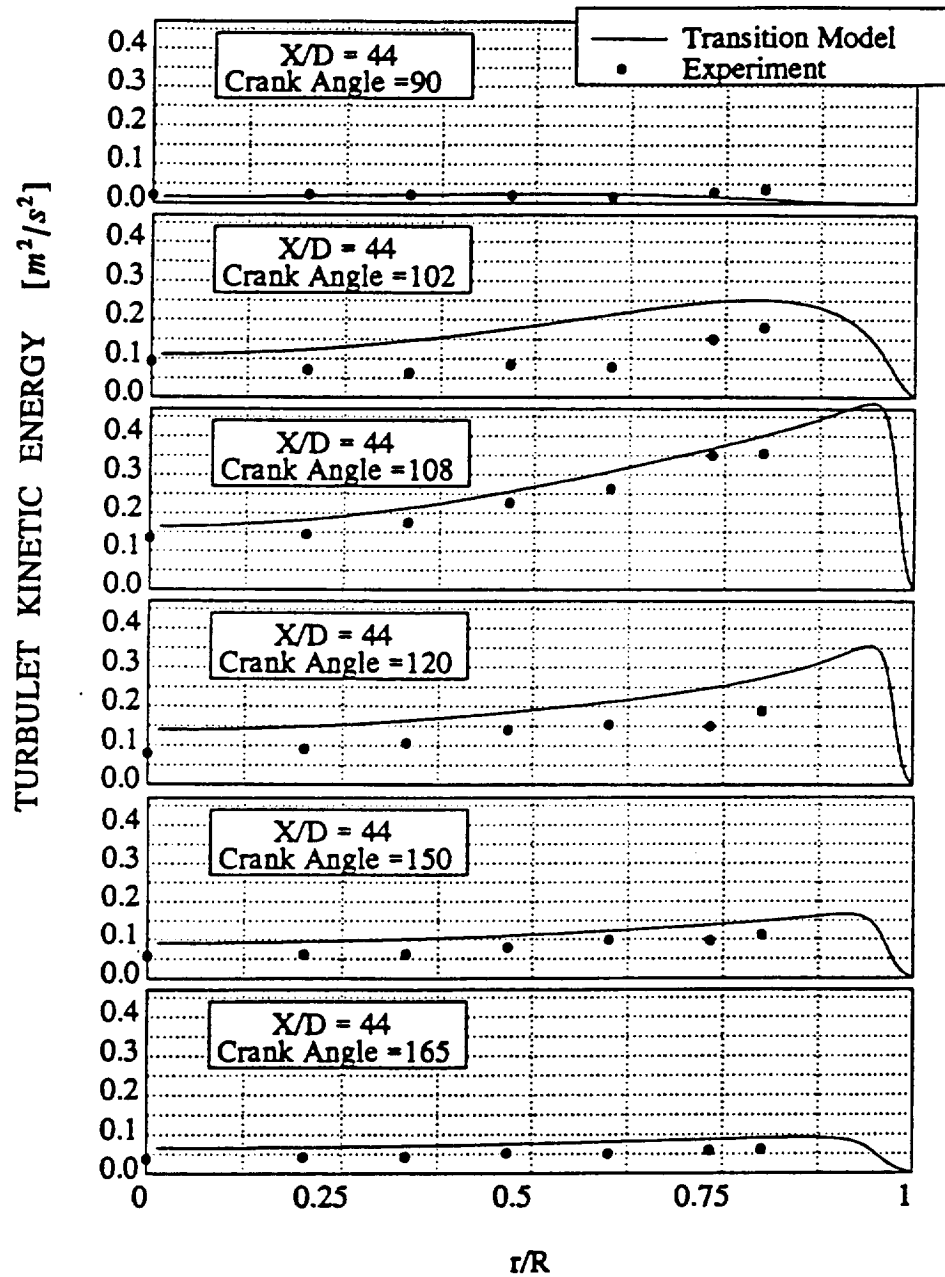


Figure 6.4c. Turbulent kinetic energy (k) profile for oscillatory pipe flow at $X/D = 44$.

data. In the turbulent portion of the cycle the Turbulent Model predicts a skin friction factor which is in good agreement with the experimental data. Using this model the position of transition is predicted at the same crank angle in the whole tube, at about $\theta = 60^\circ$, (as seen in Figure 6.5), which is not in agreement with the experiment. Utilizing the Transition Model, the location of transition is predicted accurately in the tube. Moreover, the agreement between the model's prediction for C_f and the data is excellent in the laminar part of cycle and good in the turbulent part of the cycle. Figure 6.6 shows plots similar to Figure 6.5, where the friction velocity U^* is presented instead of the skin friction factor. By definition

$$U^* = \sqrt{\frac{\tau_w}{\rho}} \quad (6.4)$$

the friction velocity is proportional to the square root of the wall shear stress value, so that the average instantaneous velocity is not used as the normalization factor as in the definition of the skin friction factor (eq. 6.3). Therefore values of U^* are close to zero at crank angles near $\theta = 0^\circ, 180^\circ$. Moreover, the agreement between the Transition Model and the experiment is excellent not only in the laminar portion of cycle but also in the turbulent portion.

From the results presented on figures 6.5 and 6.6 and from the above discussion, one can see that the numerically predicted values are in excellent agreement with the experiment. Once again, the Transition Model shows the ability to accurately determine the location of transition throughout the cycle.

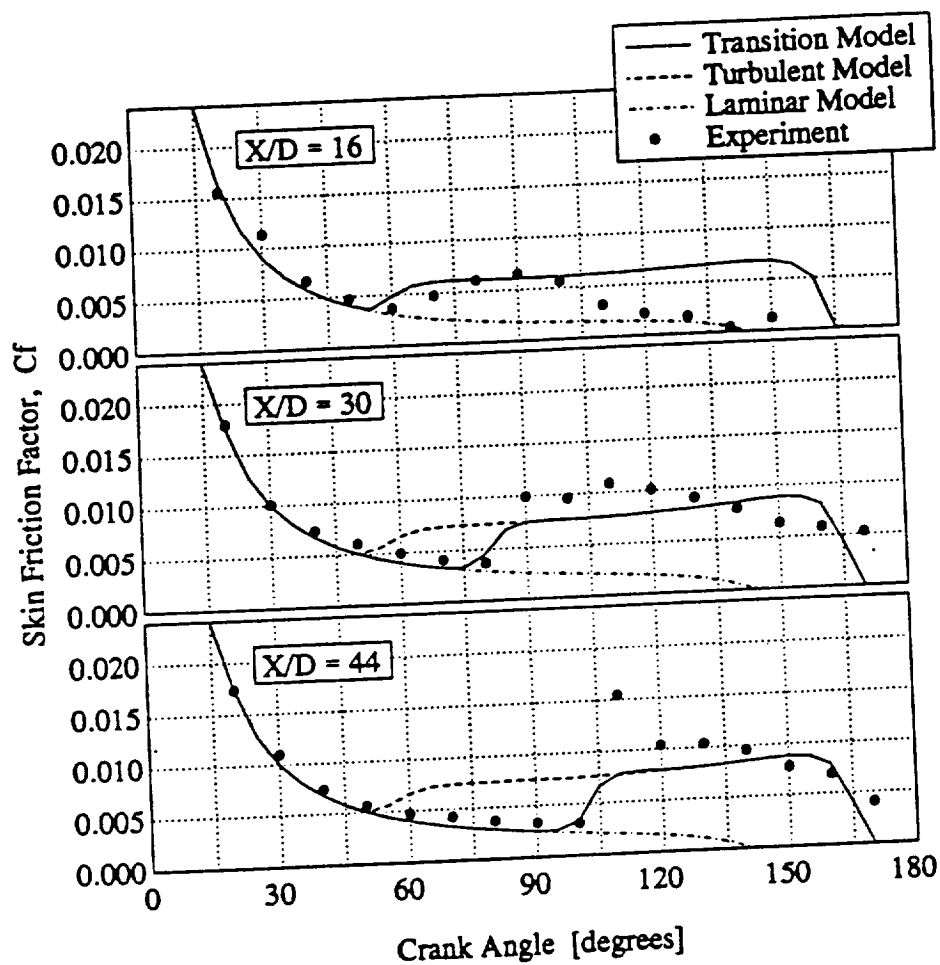


Figure 6.5. Skin friction factor (C_f) predictions from the Turbulent Model, the Transition Model, the Laminar Model, and the experiment for oscillatory flow ($Re_{max} = 11840$, $Va = 80.2$, $L/D = 60$) at $X/D = 16$, 30 , 44 locations.

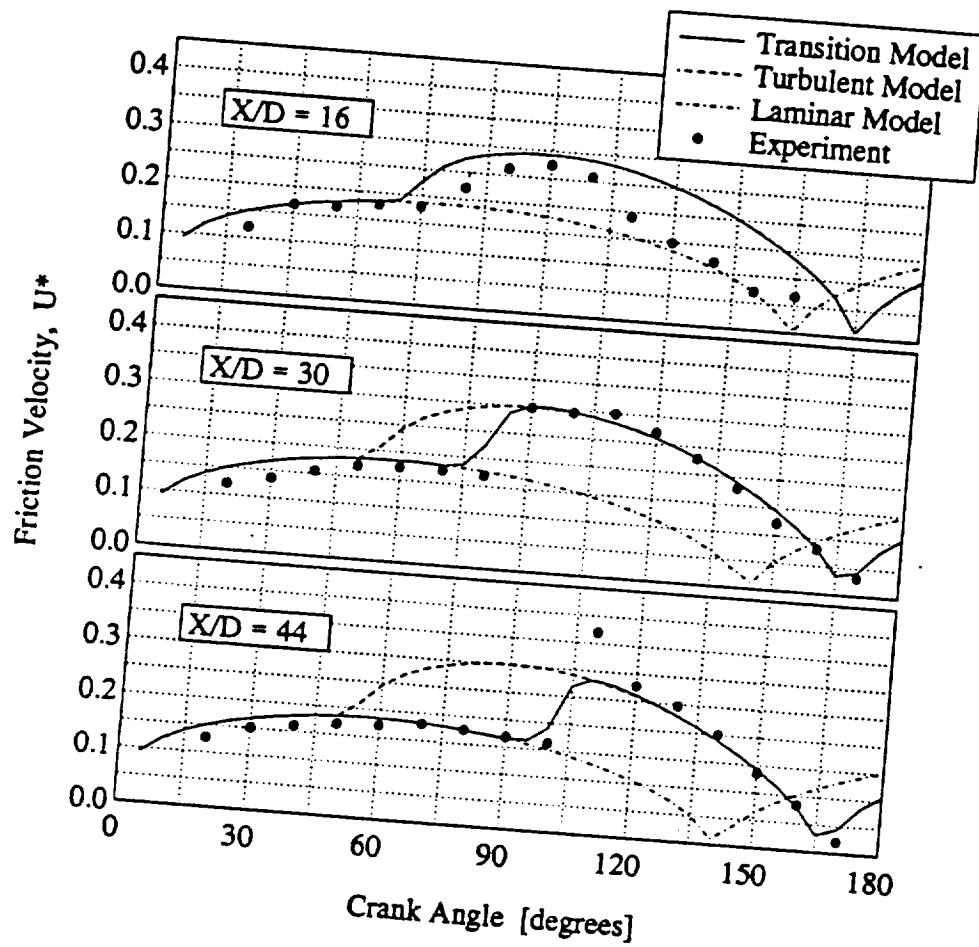


Figure 6.6. Friction velocity (U^*) predictions from the Turbulent Model, the Transition Model, the Laminar Model, and the experiment for oscillatory flow ($Re_{max} = 11840$, $Va = 80.2$, $L/D = 60$) at $X/D = 16$, 30 , 44 locations.

(6.3) Heat transfer

(6.3.1) Description of the Experiment

The experimental setup at the University of Minnesota has been utilized to obtain heat transfer data. In addition to the fluid flow experimental setup described in Section (6.1), two heat exchangers were installed at the ends of the tube with a heating element wrapped along the tube in between. The temperature measurements were made at three different axial locations $X/D = 1$, 11 and 31 , along the tube length ($L = 62D$). Via accurate temperature measurements made near the wall at all crank angles, and by extrapolating those temperature profiles, the wall temperature and the wall heat flux were obtained, (see Simon (1993) for further details). The wall temperature values are summarized here in Table 6.2. Also, inlet working fluid temperature was measured and found to be constant throughout cycle ($T_{inflow} = 21^{\circ}C$).

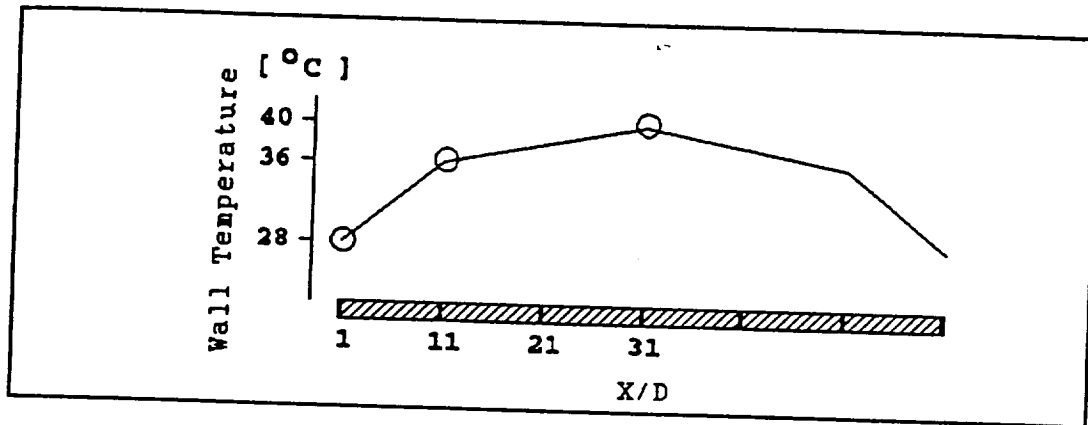
Axial Position	$X/D = 1$	$X/D = 11$	$X/D = 31$
Wall Temperature	$28^{\circ}C$	$36^{\circ}C$	$40^{\circ}C$

Table 6.2. The measurements of the wall temperature.

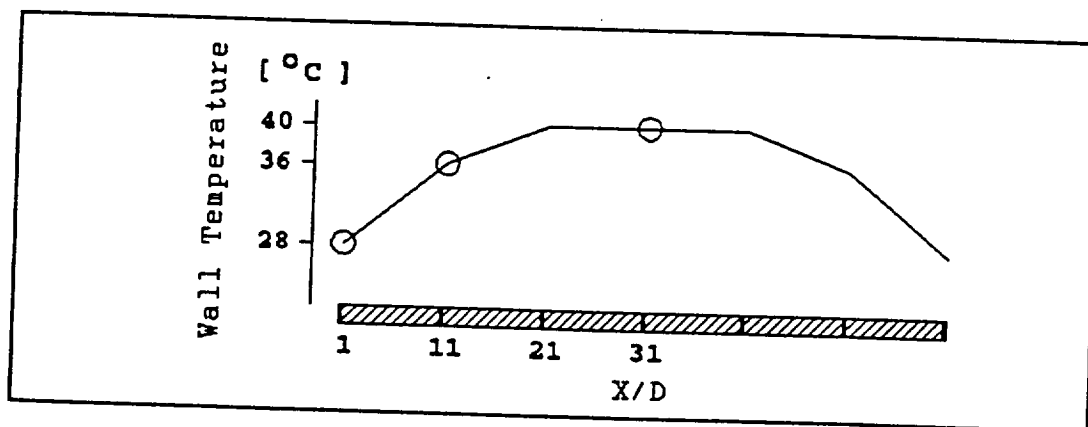
(6.3.2) Numerical Predictions

From several computational experiments, it was found that the numerical results are very sensitive to the temperature at the wall boundary, and to the initial

temperature inside the tube. From experimental data obtained from (Simon (1993)), and listed in Table 6.2) two different estimates of wall temperature distribution, presented on Figure 6.7, were chosen.



WALL BOUNDARY CONDITIONS (BC I)



WALL BOUNDARY CONDITIONS (BC II)

Figure 6.7. Wall temperature distribution.

The boundary condition (BC I), is defined by connecting the experimental temperature

points with straight lines, assuming the maximum value of wall temperature ($T_{wall} = 40^\circ$) occurs at the midpoint of the tube length. On the other hand, the boundary condition (BC II), is assumed to experience a temperature plateau, with $T_{wall} = 40^\circ$ in the middle one-third of the tube. In regard to the initial temperature profile inside the tube, the situation is more complex than in the fluid flow case. The fluid flow calculations were conducted assuming that complete mixing was taking place at the end of the cycle and a uniform inflow velocity distribution was adequate. Accordingly, the laminar flow calculations were not affected by the previous half cycle turbulent calculations. However, the temperature field calculations at the end of first cycle depend upon the amount of turbulence left in the tube at that time. In the next half cycle, that temperature field taken as the initial condition, affects the laminar (and later on the turbulent) thermal field. Therefore, several cycles are necessary to obtain a complete thermal field solution with the understanding that the laminar flow thermal field is affected by the previous half-cycle turbulent thermal field.

(6.3.3) Temperature Profiles

Figure 6.8 shows the midplane temperature profiles from computations and the experimental data at different crank angles, using BC I in this computation. (Only a slight difference was noticed in the temperature profile using either BC I or BC II.) The predicted values of temperature match the experiment close to the wall, but in the core flow these values are lower than the experimental data. Near the wall the predictions are

in close agreement with the experiment since the computed wall temperatures match the values of wall temperature obtained experimentally. However, in the core of the tube the disagreement is attributed to the turbulence model used. Notice that the turbulent temperature predictions (e.g. $\theta = 90^\circ$) are not in agreement with the data. Consequently, the end of the cycle thermal field (also the initial thermal field of the following cycle) does not match the experiment. This results in disagreement between the computational results and the experimental data in the laminar portion the of cycle.

In addition the temperature profiles at two other axial locations are presented in Figures 6.9a and 6.9b. Because the relative amplitude of the fluid displacement is ($A_r = 1.22 > 1.0$), which means that the fluid is displaced more then the length of the tube, the slug of cold fluid penetrates most of the tube. At $X/D = 16$, the temperature at the center line drops down to the inflow temperature ($T_{inflow} = 21^\circ C$) after $\theta = 30$. At $X/D = 44$, in the laminar portion of cycle, the centerline temperature rises, later drops down when a cold turbulent slug arrives, and rises again when the turbulent flow decelerates. The numerical results in the laminar portion of cycle can be further improved by making the temperature field at the beginning of the cycle more accurately reflect the actual running conditions in the experiment.

(6.3.4) Wall Heat Flux

Figure 6.10 shows the calculated and experimental data of the wall heat flux vs crank angle at the midplane. The calculations are made with the Transition Model using

two different boundary conditions (BC I and BC II) generated from wall temperature measurements. The agreement with the experimental data in both cases is excellent in the turbulent flow regime and good in the laminar flow one. Using BC I, higher values of the wall heat flux were obtained. This is expected, because BC I implies that fluid arrives at the midplane with a lower temperature than when using BC II. At the beginning and end of each half cycle the difference in the heat flux between BC I and BC II is small. Figure 6.11a shows the calculated values of the wall heat flux vs crank angle, at the axial location $X/D = 16$. At this location the flow becomes turbulent at a lower crank angle (i.e. earlier), so the maximum values of wall heat flux for both boundary conditions are shifted to lower crank angles. Figure 6.11b shows the wall heat flux data vs crank angle at $X/D = 44$. At this location the heat flux values are lower, because the arriving fluid is warmer than at the midplane. This low heat flux occurs despite the fact that the wall temperature is lower than $T_{wall} = 40^\circ$ which occurs, (see Figure 6.7) at the midplane.

Using experimental data documented in Seume et al (1992), and Simon and Qiu (1993 a,b), a one dimensional model (1-D Model) for estimating laminar and turbulent wall heat flux in oscillatory pipe flow has been formulated by Ibrahim et al (1993). In this model for the laminar portion of the cycle, the wall heat flux is calculated using the Smith and Spalding method as:

$$q_L'' = 1.43 Pr Va^{0.5} \frac{\lambda(T_w - T_{sk,L})}{D} \sqrt{\frac{\sin^3(\theta)}{2 + \cos^3(\theta) - 3\cos(\theta)}} \quad (6.5)$$

For the turbulent heat flux, the largest value from the following two equations has been

used:

$$q_T'' = 0.021 Pr^{0.6} Re^{0.8} \frac{\lambda(T_W - T_{sk,T})}{D} \sin^{0.8}(\theta) \quad (6.6)$$

$$q_T'' = 0.03 \rho c_p U'_{rms} (T_W - T_{sk,T}) \quad (6.7)$$

where $(T_{sk,L})$ and $(T_{sk,T})$, are the laminar and the turbulent sink temperatures, (see Ibrahim et. al. (1993)). Figure 6.12 shows the 1-D Model predictions for the wall heat flux at the midplane of the tube. In the figure, the experimental data and results from the Transition Model are presented. The 1-D Model predictions are seen to be good in the turbulent part, while agreement is fair in laminar flow. As expected the Transition Model performance is better than the 1-D Model. This 1-D modeling analysis was done in an attempt to avoid using extensive two-dimensional computations, and with the intent of being utilized in 1-D Stirling Engine Design Codes. As expected, the 1-D Model masks many physical details that are better described by a 2-D Model. However, it is surprising that the 1-D Model solution shows considerable success.

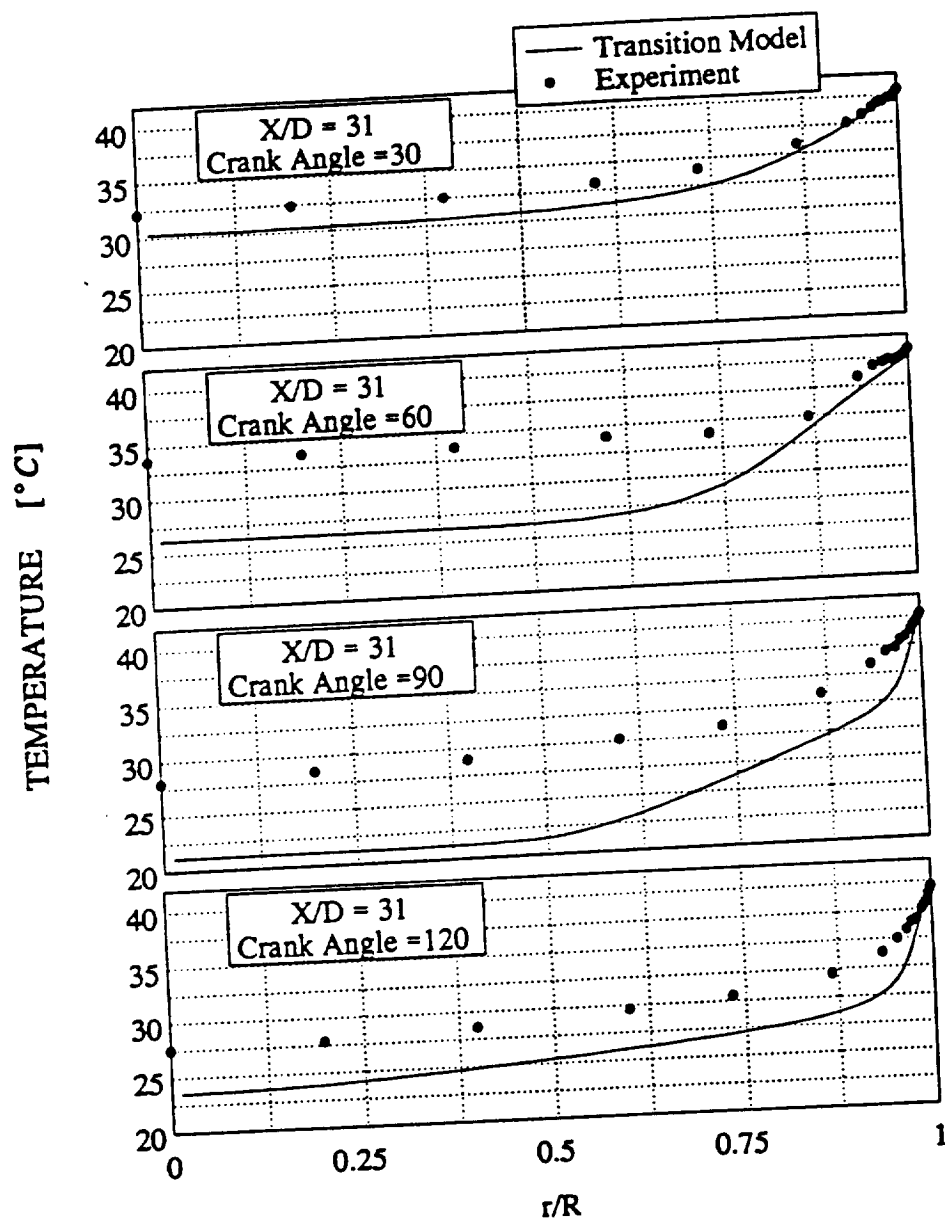


Figure 6.8. Temperature profile at midplane from Transition Model prediction and the experiment.

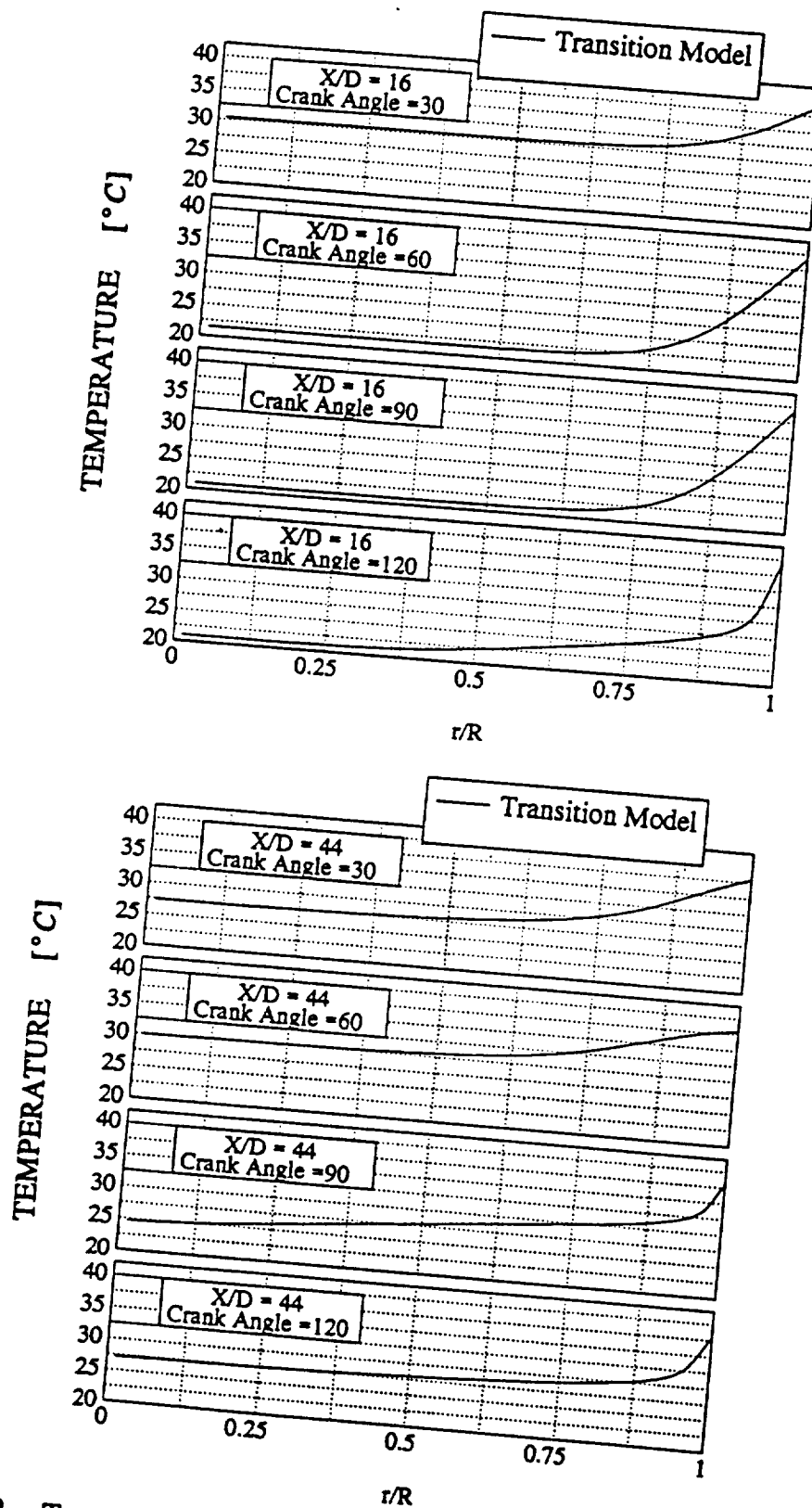


Figure 6.9. Temperature profile at a) $X/D = 16$, b) $X/D = 44$.

ORIGINAL PAGE
 GEF 2001 00117

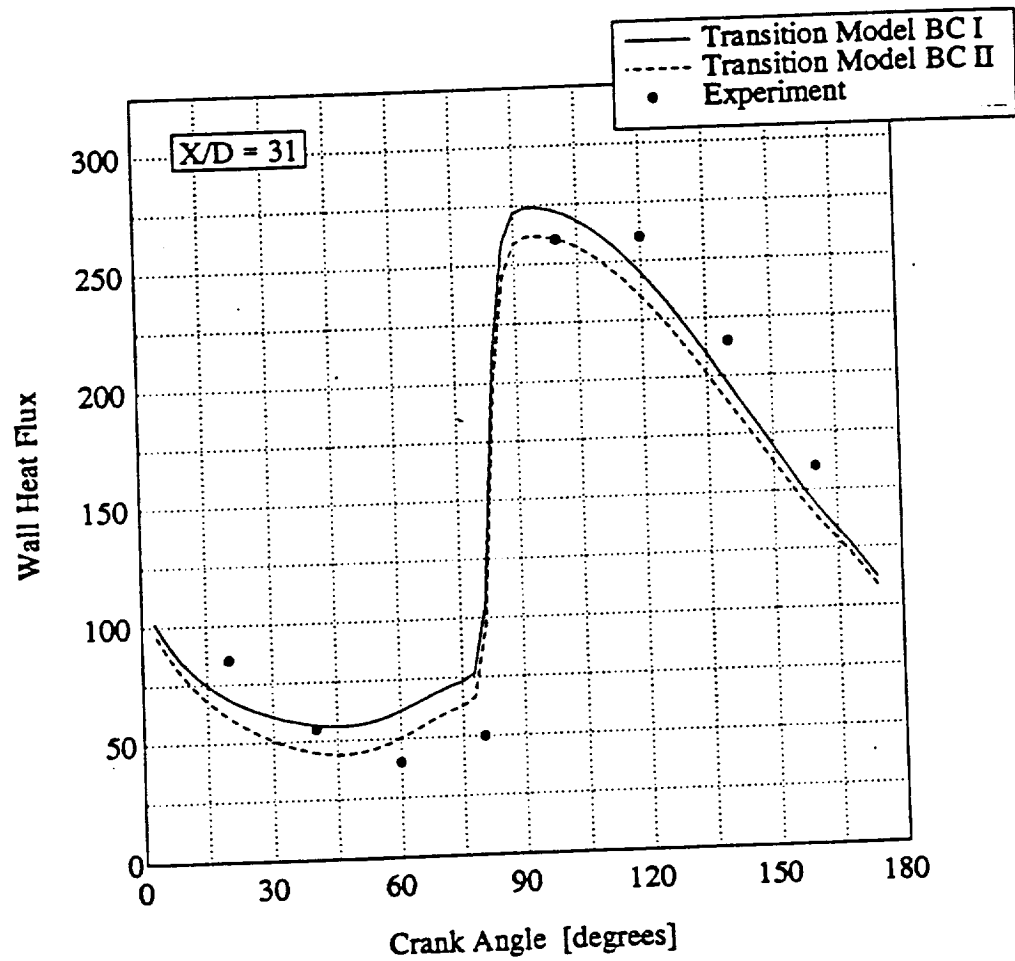


Figure 6.10. The wall heat flux at the midplane.

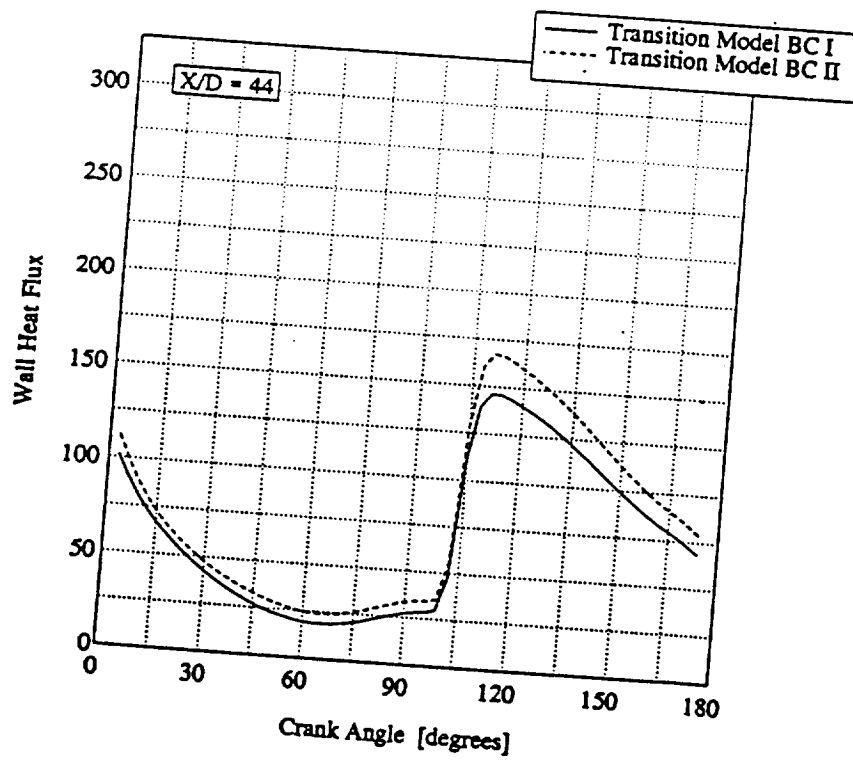
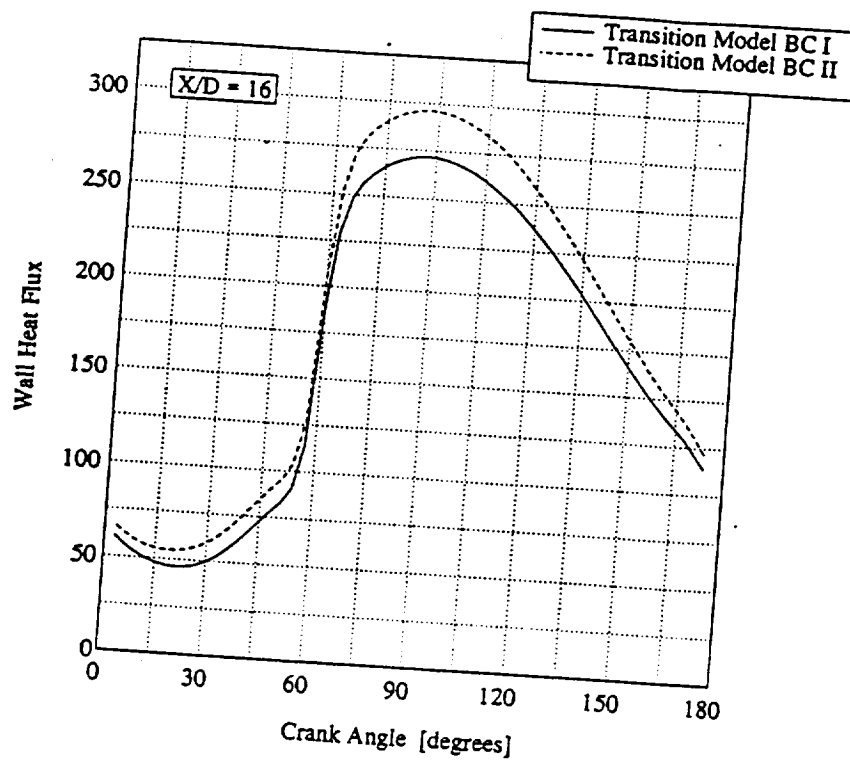


Figure 6.11. The wall heat flux at a) $X/D = 16$, b) $X/D = 44$.

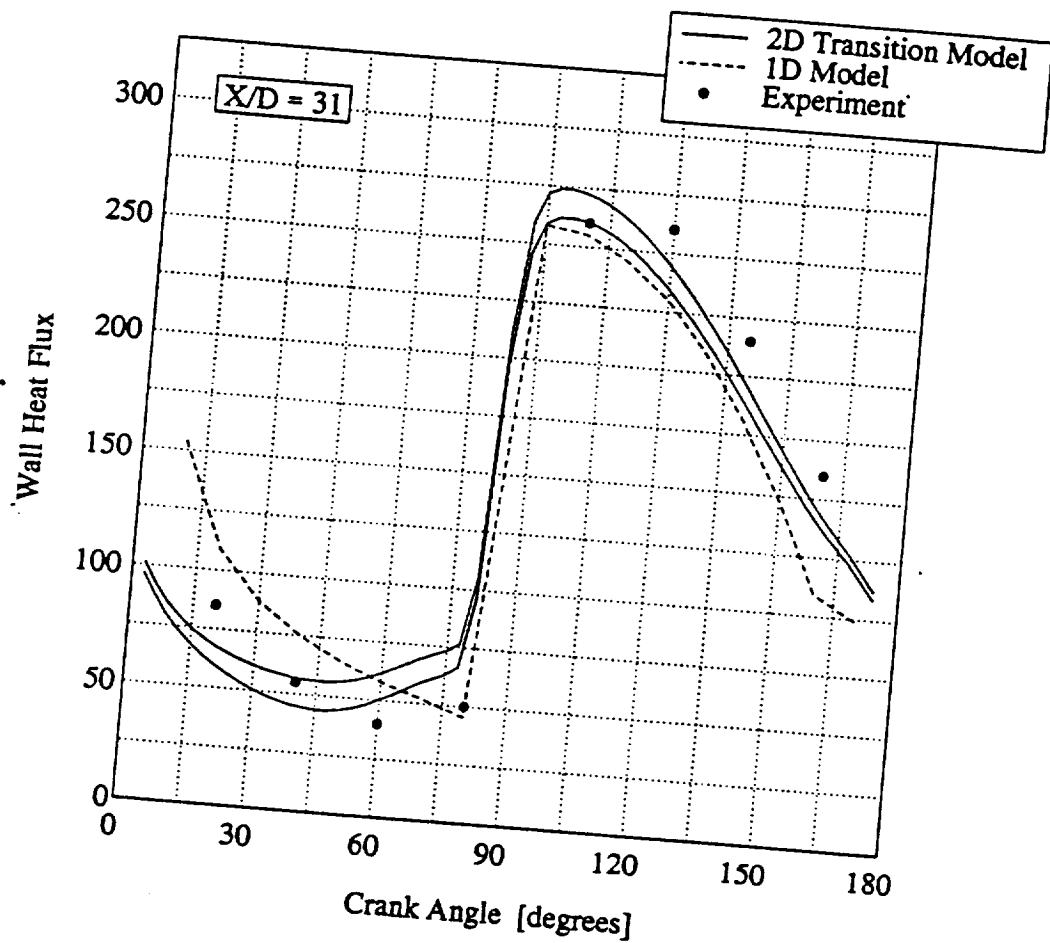


Figure 6.12. Comparison of the wall heat flux at the midplane between the experimental data, 1-D Model and the Transition Model.

CHAPTER VII

Closure

(7.1) Summary and Conclusions

(1) Numerical scheme

The code used in this study is based on the C.A.S.T. (Computer Aided Simulation of Turbulent Flows) code developed by Peric and Scheuerer (1989), which was modified to solve for unsteady oscillatory flow with zero mean velocity. Regarding the oscillation, the acceleration and deceleration of the fluid is accounted for by specifying the inflow axial velocity; and the flow in the inlet and the outlet boundary planes is switched at the half cycle (180°) and the end of each cycle (360°).

(2) Turbulence modeling

The Low Reynolds Number (Lam-Bremhorst) $k-\epsilon$ turbulent model was

introduced, in order to improve fluid flow and heat transfer calculations in the near wall region. The High Reynolds number $k-\epsilon$ model, which was originally used in the C.A.S.T. code was found not be accurate enough for solving the laminar and turbulent portions of the oscillatory flow. Moreover, an empirical transition model was utilized to activate the low Reynolds turbulence model at the appropriate time within the cycle for the axial location within the tube. In the computations a 60 (axial) by 70 (radial, half of the pipe) grid was used for all unsteady cases with the grid density being higher near the wall and lower toward the core, and a uniform grid density in the axial direction. The convergence criterion was set as a 0.1% of the global residual norms for every dependent variable. For each case 120 time steps per cycle were used. A typical run involved approximately 2000 seconds of CPU time per cycle on a Cray XMP supercomputer.

(3) Code validation

The developed numerical code performance as well as the turbulence model was validated for steady-state fluid flow and heat transfer cases. The study was conducted for steady state pipe flow with uniform inflow velocity distribution for four values of Reynolds number ($Re = 500, 5000, 15000, \text{ and } 50000$).

To insure that fully developed conditions were achieved, a tube length of 120 diameters was chosen. The Low Reynolds Number turbulence model was found to be in excellent agreement with the universal velocity profile from the law of the wall for all flow types studied. The Laminar Model (with no turbulence

modeling), and the High Reynolds Number turbulence model were found to perform well in laminar and turbulent flow types respectively. In the steady state flow with heat transfer cases, the calculated Nusselt number values were compared with the analytical results. The study was conducted for steady state laminar flow ($Re = 500$), and transition flow ($Re = 15000$) in the tube with constant wall temperature. To insure a fully developed temperature profile, the tube with a length 300 diameters was chosen. The value of the Nusselt number predicted by the Laminar Model for the laminar flow case was greater by 6% than the analytical solution. The low Reynolds $k-\epsilon$ model showed the same accuracy in calculating Nu for the laminar flow case. For the turbulent flow case the difference between the Low Reynolds Number Turbulence Model and the analytical solution was 20%. Such a large difference can be attributed to inaccuracy of the turbulence modeling.

(4) Unsteady fluid flow

The oscillating flow dimensionless parameters, $Re_{max} = 11840$, $Va = 80.2$, $L/D = 60$, and $A_r = 1.22$, were chosen to match the Space Power Demonstration Engine (SPDE) operating conditions. The computational results for: (1) normalized velocity profiles (U/U_o vs r/R), (2) dimensionless velocity profile (U^* vs Y^*), (3) turbulent kinetic energy (k vs r/R), (4) skin friction factor (C_f vs θ), and (5) friction velocity (U^* vs θ), were

compared with the experimental data at three axial locations within the tube ($X/D = 16, 30, \text{ and } 44$). The agreement between the Low Reynolds Number $k-\epsilon$ model, with an empirical transition model, and the experiment is excellent in the laminar portion of the cycle and good in the turbulent portion. Moreover, the location of transition has been predicted accurately.

(5) Unsteady fluid flow with heat transfer

The heat transfer predictions were made for the same fluid flow conditions as those described above, with constant fluid temperature at the tube inlet and nonuniform temperature distribution at the tube wall. The predicted temperature profile and wall heat flux at the midplane were compared with the experimental data. Near the wall, the predicted temperature profile was in close agreement with the experimental values, but in the core of the tube some disagreement was noticed due to difficulty in defining the initial and boundary conditions of the fluid temperature and to the turbulence model used. The wall heat flux calculations were found to be in excellent agreement with the experimental data in the turbulent flow regime and in good agreement in the laminar one.

(6) Comparison with 1-D model

Since the wall heat flux predictions match the experimental data, the Low Reynolds Number $k-\epsilon$ model, with the empirical transition model, can be used for testing the much simpler and less accurate one-dimensional models (used for 1-D Stirling Engine design codes), by generates wall heat flux values at different operating parameters than those of the experimental conditions used herein.

(7.2) Recommendations for Future Research

The principal objective of this research was to develop a numerical model capable of predicting heat transfer in a straight tube in which an oscillatory flow occurs. In order to better understand the oscillating flow heat transfer in the Stirling engine heat exchanger some suggested areas for future studies are outlined below;

- ☐ Introduce turbulent viscosity corrections so that the relaminarization process which occurs at the end of each half cycle can be modeled.
- ☐ Examine oscillating turbulent flows in a channels with a sudden change in cross-section.
- ☐ Examine the heat transfer in the complete heat exchanger components used in the Stirling engine such as the; heater, regenerator and cooler.

One can always expect to find other areas of interest within the problem. The author anticipates that the data provided from this research will be helpful for future investigations on this subject.

REFERENCES

- Ahn, K.H. and Ibrahim, M.B. (1992): *Laminar/Turbulent Oscillating Flow in Circular Pipes*, Int.J.Heat and Fluid Flow, Vol.13,No.4,pp.340-346.
- Batcheler, G.K., Townsend, A.A. (1948): *Decay of Isotropic Turbulence in the Initial Period*, Proc. Roy. Soc. A. Vol.193. pp.539-558.
- Champagne, F.H., Harris, V.G., Corrsin, S. (1970): *Experiments on Nearly Homogeneous Turbulent Shear Flow*, J.Fluid Mech. Vol.41. pp.81-141.
- Eckmann, D.M., and Grotberg, J.B., (1991): *Experiments on Transition to Turbulence in Oscillatory Pipe Flow*, J. of Fluid Mech., Vol.222, pp.329-350.
- Hino, M., Kashiwayangi, M., Nakayama, A., Hara, T. (1983): *Experiments on the Turbulence Statistics and the Structure of a Reciprocating Oscillatory Flow*, J.Fluid Mech., Vol.131, pp. 363-400.
- Ibrahim, M., Bauer, C., Simon, T.W., Qiu, S. (1993): *Modeling of Oscillatory Laminar, Transitional and Turbulent Channel Flows and Heat Transfer*, Submitted for presentation.
- Iguchi, M., Ohmi, M., and Maegawa, K. (1982): *Analysis of Free Oscillating Flow in a U-Shaped Tube*, Bull JSME, Vol.25, n 1703-1740, pp. 1398-1405.
- Jones, W.P., Launder, B.E. (1972): *The Prediction of Laminarization with a Two-Equation Model of Turbulence*, Int. J. Heat Mass Trans. Vol.15. pp.301-314.
- Jones, W.P., Launder, B.E. (1974): *The Calculation of Low-Reynolds Number Phenomena with a Two-Equation Model of Turbulence*, Int. J. Heat Mass Trans. Vol.16. pp.1119-1130.
- Kannapareddy, M. (1993): *Numerical Thermal Analyses of Heat Exchangers for The Stirling Engine Application*. Master Thesis, Cleveland State University, Cleveland, Ohio.
- Kays, W.M. and Crawford, M.E. (1993): *Convective Heat and Mass Transfer*, McGraw-Hill, 3rd Ed., 1993.

- Koehler, W.J. (1990): *Numerical Prediction of Turbulent Oscillating Flow and Associated Heat Transfer*, Ph.D. Thesis, University of Minnesota, Minneapolis, Minnesota.
- Lam, C.K., Bremhorst, K. (1981): *A modified Form of the $k-\epsilon$ Model for Predicting Wall Turbulence*, J.Fluids Eng. Vol.103. pp.456-460.
- Launder, B.E., Spalding, D.B. (1974): *The Numerical Computation of The Turbulent Flows*, Computer Methods in Applied Mechanics and Engineering, pp.269-289.
- Mayle, R.E., (1991): *The Role of Laminar-Turbulent Transition in Gas Turbine Engines*, ASME Paper 91-GT-261, Presented at the International Gas Turbine and Aeroengine Congress and Exposition, Orlando, FL, June 1991.
- Munson, B.R., Young, D.F., Okiishi, T.H. (1990): *Fundamentals of Fluid Mechanics*, John Wiley & Sons, 1990.
- Ohmi, M., Iguchi, M., and Urahata, I. (1982): *Flow Patterns and Frictional Losses in an Oscillating Pipe Flow*, Nihon Kikaigakkai (Bulletin of the JSME), Vol.25, No.202, pp.536-543, April.
- Patel, V.C., Rodi, W., Scheurer, G. (1985): *Turbulence Models for Near Wall and Low-Reynolds Number Flows: a Review*, AIAA J. Vol.23, pp 1308-1319.
- Patankar, S.V. (1980): *Numerical Heat Transfer and Fluid Flow*. Hemisphere Publ.Co., Washington.
- Patankar, S.V., and Oseid, K. (1992): *Numerical Prediction of the Heat Transfer in Transitional and Turbulent Oscillatory Flows*. Progress Report submitted to NASA Lewis Research Center, August 1992.
- Patankar, S.V., and Spalding, D.B., (1972): *A Calculation Procedure for Heat, Mass and Momentum Transfer in Three-Dimensional Parabolic Flows*. Int. J. Heat Mass Transfer, Vol. 15, pp.1787-1806.
- Peric, M., and Scheuerer, G., (1989): *CAST - a Finite Volume Method for Predicting Two-Dimensional Flow and Heat Transfer Phenomena*, GRS-Technische Notiz SRR-89-01.
- Richardson, E.G., and Tyler, E. (1929): *The Transverse Velocity Gradient near the Mouths of Pipes in which an Alternating or Continuous Flow of Air is Established*, Proc.Phys.Soc. London, Vol.42, Part 1.

- Seume, J.R., (1988): *An Experimental Investigation of Transition in Oscillating Pipe Flow*, Ph.D. Thesis, Mechanical Engineering Department, University of Minnesota, Minneapolis, Minnesota.
- Seume, J., Friedman, G., and Simon, T.W. (1992): *Fluid Mechanics Experiments in Oscillatory Flow*, NASA CR-189127.
- Simon, T.W., Ibrahim, M., Kannapareddy, M., Johnson, T., Friedman, G. (1992): *Transition of Oscillatory Flow in Tubes: An Empirical Model for Application of Stirling Engines*. 27th International Energy Conversion Engineering Conference, Vol. 15.pp.495-502., San Diego, CA, August 1992.
- Simon, T.W. (1993): *Private Communication with Professor T.Simon of University of Minnesota*. July, 1993.
- Simon, T.W., and Qiu, S. (1993a): *Investigations of Heat Transfer and Hydrodynamics of Oscillating Flows*, NASA Contractor's Progress Report April, 1993.
- Simon, T.W., and Qiu, S. (1993b): *Investigations of Heat Transfer and Hydrodynamics of Oscillating Flows*, NASA Contractor's Progress Report July, 1993.
- Shih, T.H., and Lang, N.J. (1991): *A Critical Comparison of Two-Equations Turbulence Models*, NASA Technical Memorandum 105237.
- White, F.M. (1993): *Viscous Fluid Flow*, McGraw-Hill, 2nd Ed. 1993.